2005

A NEW PIEZOELECTRIC MICROACTUATOR WITH TRANSVERSE AND LATERAL CONTROL OF HEAD POSITIONING SYSTEMS FOR HIGH DENSITY HARD DISK DRIVES

Younghee Han
University of Kentucky, Yhan1@engr.uky.edu

ABSTRACT OF THESIS

A NEW PIEZOELECTRIC MICROACTUATOR WITH TRANSVERSE AND LATERAL CONTROL OF HEAD POSITIONING SYSTEMS FOR HIGH DENSITY HARD DISK DRIVES

In high density magnetic hard disk drives, both fast track seeking and extremely accurate positioning of the read/write head are required. A new piezoelectric microactuator with transverse and lateral control of the head positioning system for high density hard disk drives is proposed. First, the structure of the new piezoelectric microactuator is illustrated. Design of the new microactuator is based on the axial deformation of piezoelectric elements for lateral motion and the bimorph actuation of piezoelectric elements for transverse motion. Next, a mathematical model of the microactuator system is defined. Static properties associated with the displacement of the system are evaluated and then dynamic system equations of the system are evaluated. Frequency response of the system is studied based on the dynamic system equations of the actuator system. Dynamic properties of the system with a variety of system parameters are evaluated. Finally, the controller design for the actuator is presented. Simulation results show that the new actuator achieves a maximum stroke of displacement of more than 0.2μm with servo bandwidth of more than 5 kHz in the lateral direction and the flying height is decreased to less than 6 nm with resonance frequency of more than 100 kHz under the 0.5 % damping assumption. The new piezoelectric microactuator improves performance of high density hard disk drives by increasing servo bandwidth and decreasing flying height.

KEYWORDS: Hard Disk Drives, Piezoelectric Uniaxial Control, Piezoelectric Bimorph Control, Dual Actuator Servomechanism, Flying Height Control

Younghee Han

December 15, 2005

A NEW PIEZOELECTRIC MICROACTUATOR WITH TRANSVERSE AND LATERAL CONTROL OF HEAD POSITIONING SYSTEMS FOR HIGH DENSITY HARD DISK DRIVES

By

Younghee Han

Dr. H. S. Tzou

(Director of Thesis)

Dr. George Huang

(Director of Graduate studies)

December 15, 2005

RULES FOR THE USE OF THESES

Unpublished theses submitted for the Master's degree and deposited in the University of Kentucky Library are as a rule open for inspection, but are to be used only with due regard to the rights of the authors. Bibliographical references may be noted, but quotations or summaries of parts may be published only with the permission of the author, and with the usual scholarly acknowledgments.

Extensive copying or publication of the thesis in whole or in part also requires the consent of the Dean of the Graduate School of the University of Kentucky.

THESIS

Younghee Han

The Graduate School

University of Kentucky

2005

A NEW PIEZOELECTRIC MICROACTUATOR WITH TRANSVERSE AND LATERAL CONTROL OF HEAD POSITIONING SYSTEMS FOR HIGH DENSITY HARD DISK DRIVES

THESIS

A thesis submitted in partial fulfillment of the
requirements for the degree of Master of Science in the
College of Engineering
at the University of Kentucky

By

Younghee Han

Lexington, Kentucky

Director: Dr. H. S. Tzou, Professor of Mechanical Engineering

Lexington, Kentucky

2005

MASTER'S THESIS RELEASE

I authorize the University of Kentucky
Libraries to reproduce this thesis in
whole or in part for purposes of research.

Signed: Younghee Han

Date: December 15, 2005

ACKNOWLEDGMENTS

I would like to express my thanks to my advisor Dr. H.S. Tzou for his guidance, advice, and patience throughout my graduate school career. Next I wish to thank my complete Thesis Committee: Dr. Tingwen Wu and Dr. Mark Hanson for their advising, suggestions and review of this thesis.

I would like to thank the faculty, staff, secretaries, and graduate students of the Mechanical Engineering Department. I also want to express my thanks to the colleagues of the Structronics Laboratory: Dr. W.K. Chai and Greg DeHaven for their help and support.

Finally, I wish to thank my family for all their support and encouragement throughout my graduate school careers.

TABLE OF CONTENTS

LIST OF TABLES

LIST OF FIGURES

Chapter One

Introduction

1.1 Background

The current trend in hard disk design is towards smaller hard disks with much larger capacities. The areal density is a common factor used to show the storage capacity of hard disk drives. The areal density is represented as multiplication of linear density and track density as shown **Figure 1.1.1.**

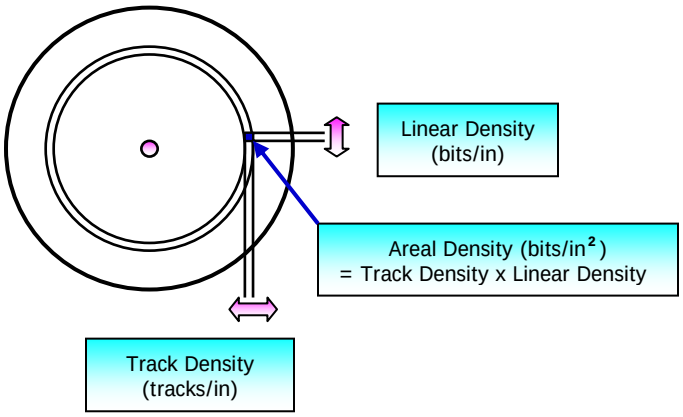

Figure 1.1.1: Areal, track, and linear density.

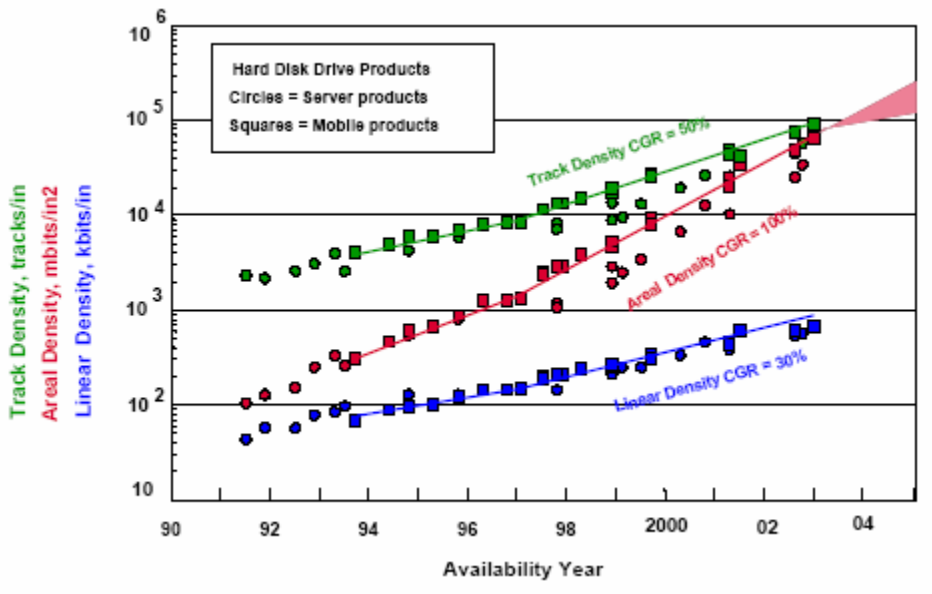

Figure 1.1.2: Areal, track, and linear density perspective (Hitachi, 2003).

As shown in **Figure 1.1.2,** areal density has been dramatically increasing at a rate of 100% a year. Hard disk drives of more than 30 Gb/in^2 areal densities are now available and research in the hard disk drives industry is now targeting an areal density of more than 100 Gb/in^2 or 1 Tb/in^2. In order to achieve such high track density, it is necessary to improve position accuracy which in performance is typically measured by the servo bandwidth, and the efficiency of the read/write mechanism of hard disk drives, which can be achieved by lowering flying height of the head. **Figure 1.1.3** shows a positioning system. A fast track seeking ensures better performance of hard disk drives.

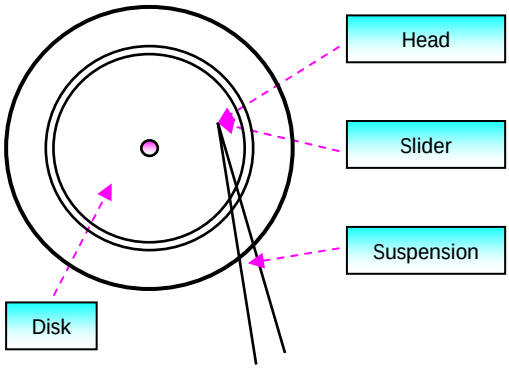

Figure 1.1.3: Head positioning system.

The performance of a positioning system is typically measured by the servo bandwidth since a positioning system with high servo-control bandwidth has low sensitivity to disturbances. The servo bandwidth is the frequency where the amplitude of the open-loop frequency response remains stable. Thus, increasing the servo bandwidth has been a critical step in increasing storage densities. Another critical step to increase the recording density of hard disk drives is achieving better performance of the read/write mechanism which is related to the flying height of the slider. The spacing between the slider and the disk as shown **Figure 1.1.4** is called the flying height.

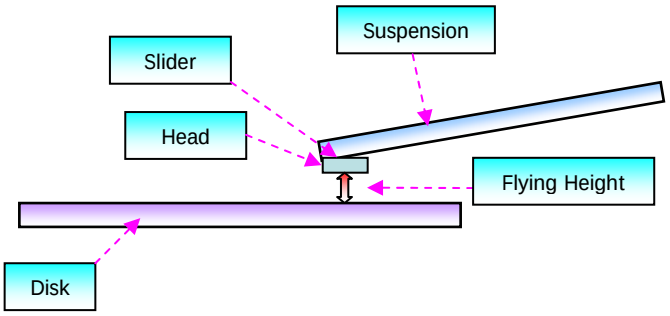

Figure 1.1.4: Flying height of the slider.

The rapid spinning of the disk creates a thin air cushion between the slider and the disk surface. This aerodynamic property allows the slider to fly above the surface. The strength of the magnetic field is proportional to the cube of the distance between the head and the disk. Thus, lowering the flying height has been a critical step in increasing storage densities. Accordingly, current research to improve performance of high density hard disk drives using smart material actuators focus on these two requirements: high servo bandwidth and low flying height. A dual actuator servo system is proposed to achieve a high servo bandwidth in the positioning system and a flying height control actuator is proposed to improve read/write mechanism of hard disk drives.

1.1.1 Dual actuator servo system

As the recording density of hard drives is increasing, more accurate and much faster head positioning servomechanisms are required. The conventional voice coil motor is considered difficult to achieve such requirements because of its large mass, low resonant frequency and nonlinear response. To provide fast and accurate positioning, a dual stage actuator system is proposed. A dual stage actuator system uses the conventional voice

coil motor as a primary actuator for track seeking and a secondary micro-actuator located between the voice coil motor and the head for track following. Because tracking accuracy and speed to response is proportional to the servo bandwidth, to achieve more accurate positioning of the head for higher track density, we need to increase the servo bandwidth. Current research on microactuator design is divided into three types according to the position where the microactuator is placed. The first type is the suspension driven actuator. The microactuator is located on a suspension, driving the suspension for head positioning. Suspension driven actuators can provide a large stroke of displacement by using the suspension length. The structure of the actuator is simple because it is relatively large and the actuator does not require a large modification to the shape of the head suspension assembly. However, the servo bandwidth is limited by the resonant frequency of the suspension. Since Lead Zirconate Titanate (PZT) has high stiffness and generates large forces when used as an actuator, PZT is commonly used in suspension driven actuators [1, 2, 3 and 4]. The second type is the slider driven actuator. The actuator is mounted in between the suspension and slider, driving a slider for head positioning. Compared to the suspension driven actuators, servo bandwidth is increased in the slider driven actuators. Slider driven actuators can also be used with existing head suspension assemblies since an actuator is placed between slider and suspension without a large modification [5, 6, 7, and 8]. The third type is the head driven actuator. The actuator is inserted between the head element and the slider, driving a head element. Since head driven actuators have extremely small size and low mass, this actuator system can achieve the highest servo bandwidth. However, since the structure of the actuator is based on micro electro mechanical system (MEMS) structure, it needs a fabrication process. Thus, this kind of actuator has low productivity. The position in which the actuator is placed may cause problems in read and write mechanism of the head [9 and 10].

1.1.2. Read/write mechanism

The rapid growth of recording density of hard-disk drives has required better read/write interface mechanisms. When the areal density of a drive is increased to improve capacity and performance, the magnetic fields are made smaller and weaker. This requires the

flying height of the slider to be made as small as possible in order to increase areal densities. Currently, the flying height for sliders is 20-25nm in 3.5" drives. However, high recording densities of hard-disk drives require the flying height of sliders to be decreased to less than 10 nm as shown **Figure 1.1.5**.

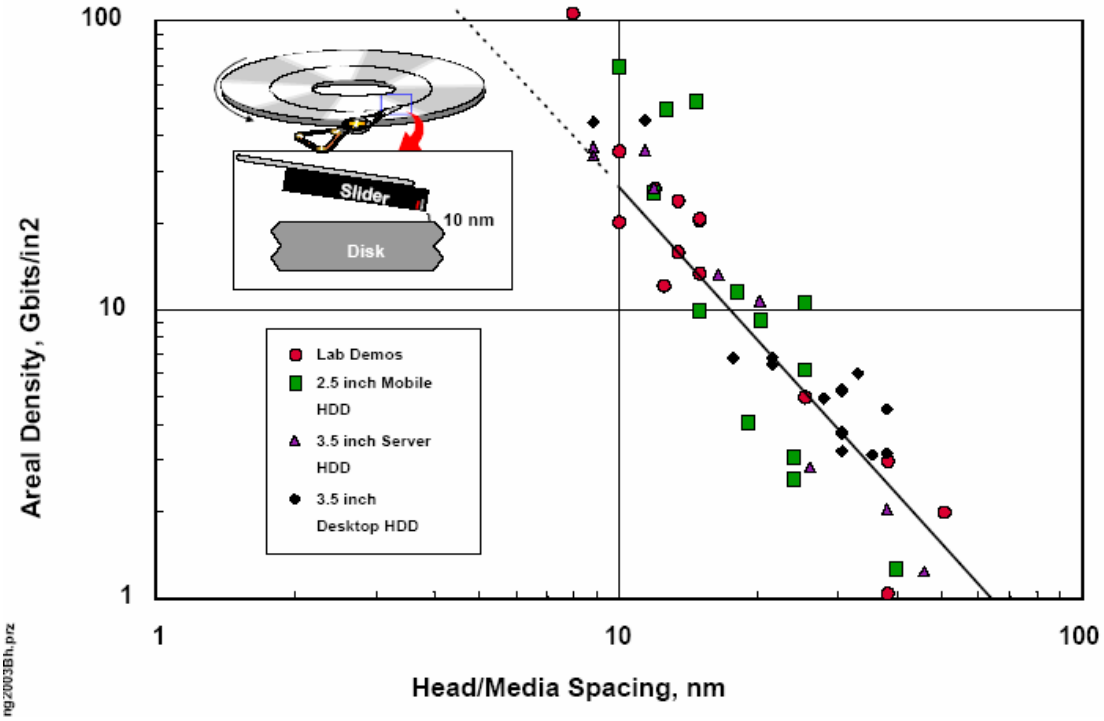

Figure 1.1.5: Flying height-areal density perspective (Hitachi, 2003).

The air-bearing method alone will not be sufficient to maintain the sub-10 nm flying height specification. Achieving such low flying height is possible by adjusting the height

of the head individually by using a microactuator. There have been many approaches to the design of flying height control actuators. A self adjusting flying height slider adjusts flying height by built in microactuator only when necessary read/write operations [11, 12, 13 and 14]. This type of slider will allow us not only to reduce the head-disk spacing during read/write operations but also to keep a safe flying height when the head is not in use, which will lead to a significant improvement of the recording density and the reliability.

1.2 Objectives and Methodology

As mentioned above, there have been many approaches to increasing recording density of hard disk drives. Research involving the use of a microactuator for the track following or the flying height adjustment has been conducted independently. The main objective of this research is to propose a new piezoelectric microactuator which improves positioning accuracy and the efficiency of the read/write mechanism by increasing the servo bandwidth and by adjusting the flying height for high density hard disk drives and evaluate their performance. Piezoelectric materials were chosen for the new actuator because of their ability to generate large forces, their fast response speed and their stiffness. However, they need high voltage input to generate the required displacement. Modifying the structure of a microactuator, which need less voltage input, is challenging. The approach to solving this design problem is to design an actuator consisting two parts, which are independently controlled for each purpose: the track following and the flying height adjustment, based on the state of the art of current hard disk drives. The uniaxial deformation of piezoelectric materials is used to generate target displacement in lateral direction and the bimorph deformation of piezoelectric materials is used to generate target displacement in the transverse direction. The analysis of the frequency response of the new actuator shows improvement of the servo bandwidth and the resonance frequency. The analysis of the time response shows the controller in closed-loop system compensates for disturbances.

1.3 Thesis Organization

This thesis has been organized into six chapters. The current chapter presented background information on research for high density hard disk drives. Chapter 2 discusses the theoretical developments for piezoelectric materials, target performances of the microactuator, structure of the microactuator and its characteristics. Chapter 3 covers the mathematical modeling of the actuator system and results of system equations. Chapter 4 goes through the frequency response of the system based on system equation and analysis of effects of the system parameters. Chapter 5 presents the time response of the system with the controller design and results. Chapter 6 concludes the thesis with a brief summary of the work and results and with a discussion about future plans for further research in this area of study.

Chapter Two

Material Selection and Structure of the New Actuator

In this chapter, general properties of piezoelectric materials are given, followed by an explanation of the specific material selection and the design concept for the new piezoelectric microactuator, after which the geometrical and electrical properties of the new piezoelectric actuator are given.

2.1 Piezoelectric Materials

Characteristics of the piezoelectric materials are presented, followed by design concepts used in the actuator design. Then, the piezoelectric material selection, which is based on the requirements for use as a microactuator in hard disk drives, is given.

2.1.1 Characteristics of piezoelectric materials

Piezoelectricity is an electromechanical phenomenon, which relates electric polarization to mechanical stress/strain in piezoelectric materials. An electric charge can be observed when the material is deformed, which is referred to as the direct effect. Application of an electric field to the piezoelectric materials can introduce mechanical stress or strain, which is named as the converse effect. **Figure 2.1.1** shows the characteristics of piezoelectric materials.

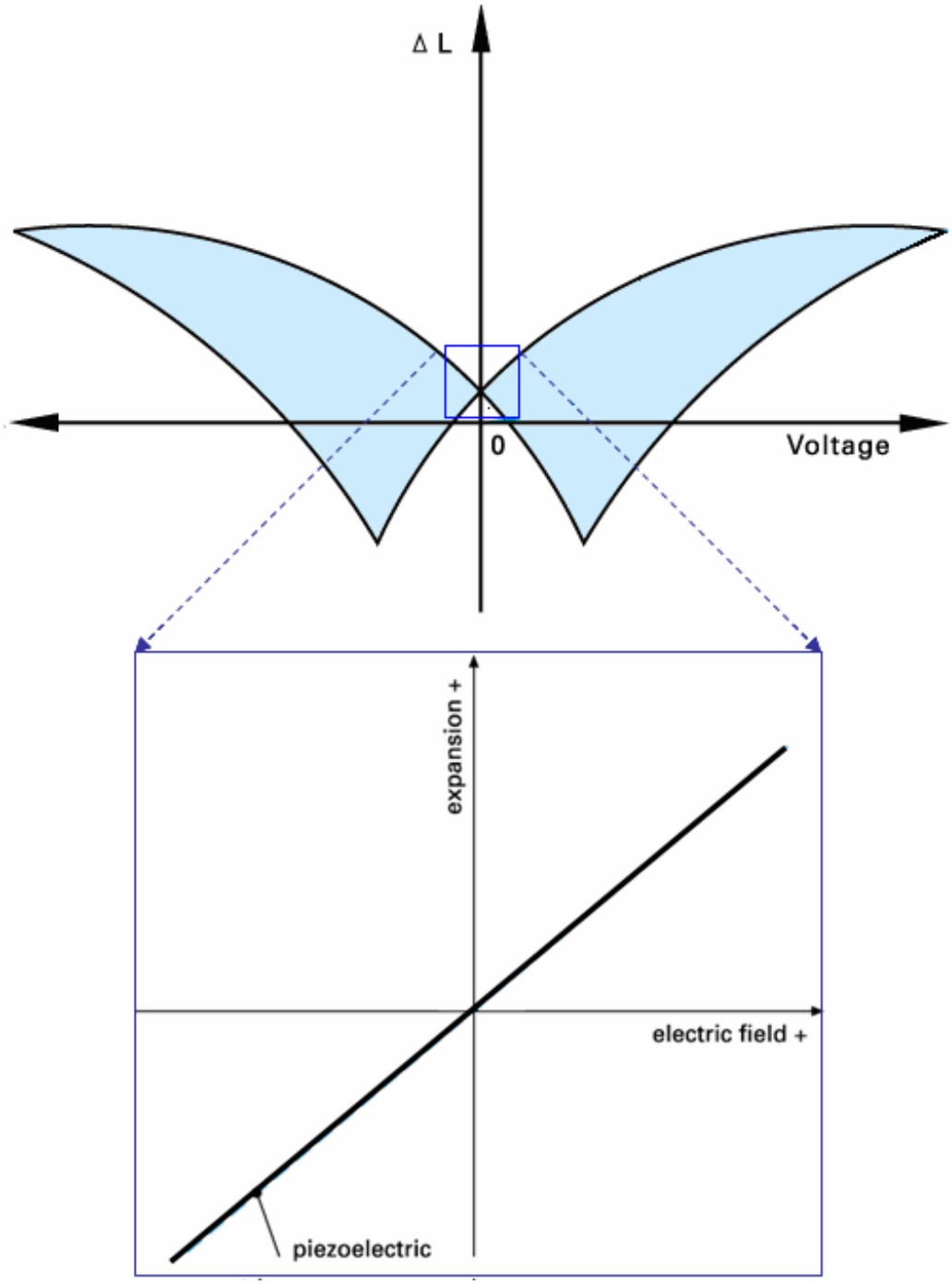

Figure 2.1.1: Piezoelectric characteristics (PI, 2005).

The piezoelectric direct effect can be expressed as

$$\mathbf{D} = \mathbf{d}\,\mathbf{T} + \boldsymbol{\varepsilon}^{T}\mathbf{E} \tag{2.1.1}$$

The piezoelectric converse effect can be expressed as

$$\mathbf{S} = \mathbf{s}^{E}\,\mathbf{T} + \mathbf{d}^{t}\mathbf{E} \tag{2.1.2}$$

where **S** is the strain tensor; **T** is the stress tensor; **E** is the electric field vector; **D** is the electric displacement vector; $\boldsymbol{\varepsilon}^{T}$ is the dielectric tensor measured at constant stress T; **d** is the piezoelectric strain constant matrix. These coefficients describe the relationship between the applied electrical field and the mechanical strain produced. $\mathbf{d}^{t}$ is the transpose of **d**; and $\mathbf{s}^{E}$ is the compliance matrix evaluated at a constant electric field.

2.1.2 Design concepts

The new piezoelectric hard disk drive actuator uses uniaxial deformation of piezoelectric materials for lateral displacement generation and bimorph deformation of piezoelectric materials for transverse displacement generation. **Figure 2.1.2** shows the deformation of piezoelectric materials. An applied electric field can cause a piezoelectric material to change dimensions.

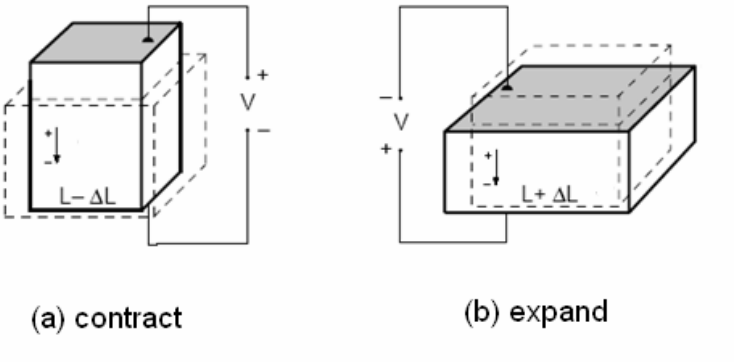

Figure 2.1.2: Axial deformation of piezoelectric materials (PIEZO SYSTEM, INC., 2005).

A piezoelectric bimorph beam is made of two piezoelectric layers with opposite polarity as shown in **Figure 2.1.3**.

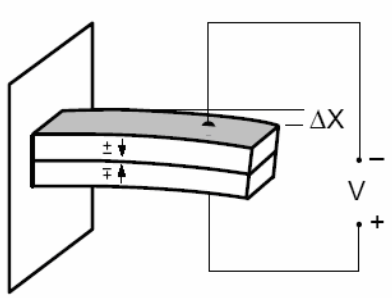

Figure 2.1.3: Bimorph deformation of piezoelectric materials (PIEZO SYSTEM, INC., 2005).

Due to the reversed polarity in these two layers, the resultant stresses in these two layers are the opposite sign when an external voltage is applied across the beam thickness. These two stresses cause a coupling effect leading to a bending of the bimorph beam. Detailed discussion will be presented in Chapter Three.

2.1.3 Material selection

Requirements for use as a microactuator in hard disk drives include lightness, stiffness, large force generation, large displacement generation and temperature stability. By considering those conditions, Lead Zirconate Titanate 5 (PZT5) is chosen for the new microactuator. Material properties of PZT5 are shown in **Table 2.1.1**.

Table 2.1.1: Material properties of PZT5 (Morgan Electro Ceramics, 2005).

Property	Symbol	Units	Value
Density	ρ_p	$\times 10^{-6}\,\mathrm{kg/mm^3}$	7.8
Young's modulus	Y_p	$\times 10^{7}\,\mathrm{mN/mm^2}$	6.7
Piezoelectric displacement coefficient	d_{31}	$\times 10^{-9}\,\mathrm{mm/V}$	-215
Curie temperature	T_C	$^{\circ}\mathrm{C}$	350

2.2 Target Performance of the Actuator

The new piezoelectric actuator consists of two actuation parts which generate a lateral displacement and a transverse displacement respectively. In this section, the target areal density and required performances of the new actuator for each direction are defined. Based on the current technology in the hard disk drives industry and current research for high density hard disk drives, the target areal density of a hard disk drive is set to $100\mathrm{Gb/in^2}$.

2.2.1 Target performance of the actuator in the lateral direction

It is expected that track density is 2.5×10^5 track/in and track pitch is $0.1\,\mu$m in 100Gb/in^2 hard disk drives. Stroke of displacement should be satisfied by a target value which is set for good tracking accuracy. The microactuator is typically required to cover more than one track's displacement range to avoid actuator saturation. Therefore, the stroke of displacement should be more than $0.2\,\mu$m ($\pm0.1\,\mu$m), corresponding to 2 tracks at a 2.5×10^5 track/in track density and 5-6 kHz of loop bandwidth will be required to enable accurate tracking up to 2.5×10^5 track/in track density [20]. **Table 2.2.1** shows the target performances of the microactuator in the lateral direction.

Table 2.2.1: Target performances of the actuator in the lateral direction.

Areal density	100 Gb/in^2
Track density	2.5×10^5 track/in
Track pitch	$0.1\,\mu$m
Stroke of displacement	$0.2\,\mu$m($\pm0.1\,\mu$m)
Bandwidth frequency	5-6 kHz
Resonance frequency	60 kHz

2.2.2 Target performance of the actuator in the transverse direction

Currently, the flying height for sliders is 20-25nm in 3.5" drives and is required to be less than 6nm flying height in 100Gb/in^2 hard disk drives as shown **Figure 1.1.5.** Therefore, the deflection of the piezoelectric bimorph beam should be more than 19nm, corresponding to 6nm flying height. The resonance frequency of the actuator is set to be more than 100 kHz. **Table 2.2.2** shows the target performances of the actuator in the transverse direction.

Table 2.2.2: Target performances of the actuator in the transverse direction.

Areal density	100Gb/in^2
Flying height	6nm
Deflection of end of beam	19nm
Mechanical resonant frequency	100kHz

2.3 Structure of the New Piezoelectric Microactuator

As mentioned in Chapter One, current research on dual actuator system design is divided into three types according to the location where the micro actuator is placed. In this thesis, the slider driven actuator in which the microactuator is placed between suspension and slider is chosen. The geometrical properties of the actuator are given, followed by electrical properties of the new actuator.

2.3.1 Geometrical properties of the actuator

The new actuator is a slider driven type, placed between suspension, which is moved by the voice coil motor (VCM), and slider. The designed piezoelectric microactuator has a simple structure as shown in **Figure 2.3.1**. The new microactuator can be used with an existing assembly with small modification.

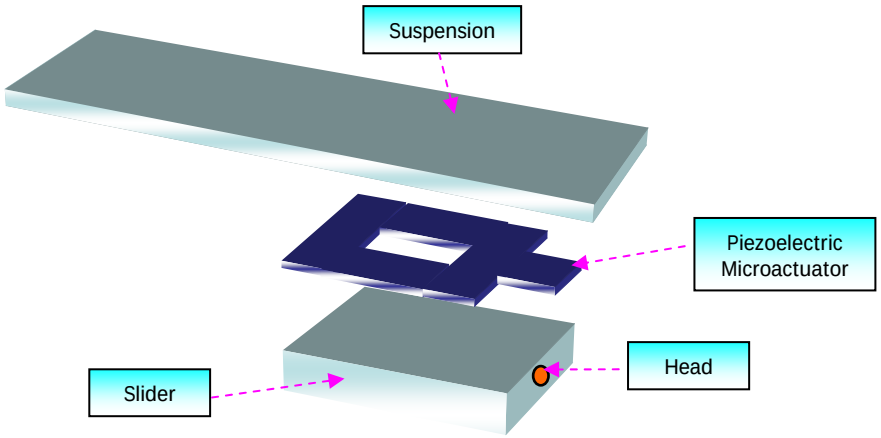

Figure 2.3.1: Location of the piezoelectric actuator.

The new actuator is designed for 3.5” hard disk drives with Pico size slider. Geometrical properties of Pico size sliders are given in the **Table 2.3.1**.

Table 2.3.1: Geometrical properties of sliders (Hitachi, 2004).

Slider Size	Mini 100%	Micro 70%	Positive Pressure Nano 62%	Negative Pressure Nano 50%	Pico 30%	Femto 20%
Intro Year	1980	1986	1991	1994	1997	2003
Dimensions, mm						
Length	4.00	2.80	2.50	2.00	1.25	0.85
Width	3.20	2.24	1.70	1.60	1.00	0.70
Height	0.86	0.60	0.43	0.43	0.30	0.23
Slider Mass, mg	55.0	16.2	7.8	5.9	1.6	0.6

The structure of the new actuator is shown **Figure 2.3.2**. The actuator is composed of two layers of PZT and one adhesive layer. The property and the effect of an adhesive layer are not considered in this study. Two piezoelectric layers add mechanical strength and stiffness to the actuator and reduce driving voltage. The new actuator has three active polarized portions, which are related to the swing motion and the bending motion, and two bonding parts in a single body. The swing assembly, which is consists of two active polarized parts, generates swing motion by using uniaxial actuation of piezoelectric

materials. The bending part generates bending motion by using bimorph actuation of piezoelectric materials. The bonding parts are used for attaching the actuator to the existing assembly. The microactuator has two bonding areas. One is mounted to the suspension and the other is glued to the slider respectively.

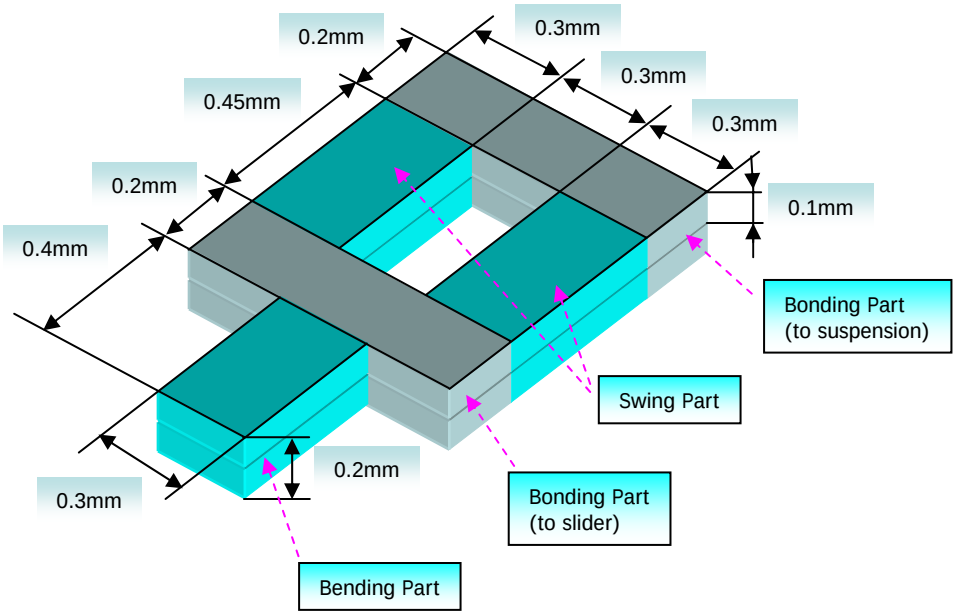

Figure 2.3.2: Structure of the piezoelectric actuator.

2.3.2 Polarization and electrodes

In this section, electrical properties of the system are given. **Figure 2.3.3** shows that how electrodes are applied.

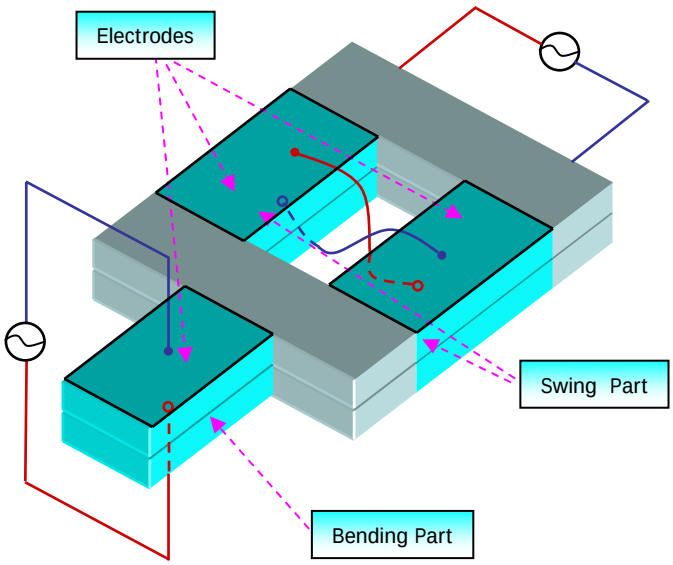

Figure 2.3.3: Electrodes and wiring.

Each actuation part has two electrode layers. Because swing motion and bending motion are independent, two signal inputs are required. In each part, a control voltage is applied across all piezoelectric layers at once. The microactuator's leads are electrically isolated so that the control voltage of the microactuator does not affect the head signal.

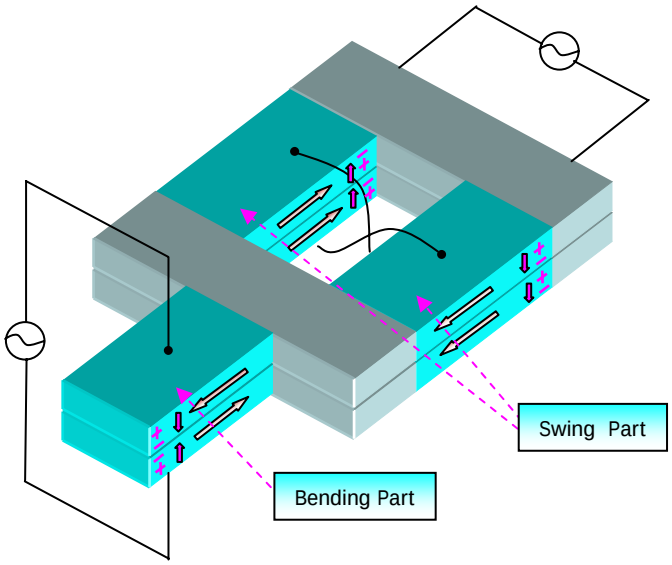

Figure 2.3.4: Polarization direction of the piezoelectric actuator.

The swing part, which relates to the lateral motion of the head, consists of two separated parts with opposite polarity. These two parts are made of two PZT layers, each of which has the same polarity. Therefore, the 2-PZT layers element in the swing part behaves like a single body. By expanding or contracting together, they generate large driving forces than one layer, reduce drive voltage by half and give high stiffness. The swing part of the actuator will be called the lateral actuator for the remainder of this thesis. The bending part of the actuator, which is made of two piezoelectric layers with opposite polarity, is related to transversal motion of the head. Since these two layers are polarized in opposite direction, input voltage results in contraction on one surface and expansion on the other surface which generate bending motion. The bending part of the actuator will hereafter be called the transverse actuator.

Chapter Three
Mathematical Modeling

In this chapter, mathematical models of the piezoelectric microactuator system are developed and results of system equations are given. Assuming there is no coupling between the transverse actuator and the lateral actuator, dynamic equations of the lateral actuator and the transverse actuator are derived independently.

3.1. System Equation of the Lateral Actuator

In this section, the maximum input drive voltage that ensures the target displacement in the lateral direction is calculated first and the dynamic system equation of the lateral actuator is defined, followed by evaluation of system parameters.

3.1.1 Maximum input voltage for the lateral actuator

Based on the target displacement which is defined in Chapter Two, the required maximum input drive voltage is calculated. **Figure 3.1.1** shows the change of dimension of piezoelectric materials.

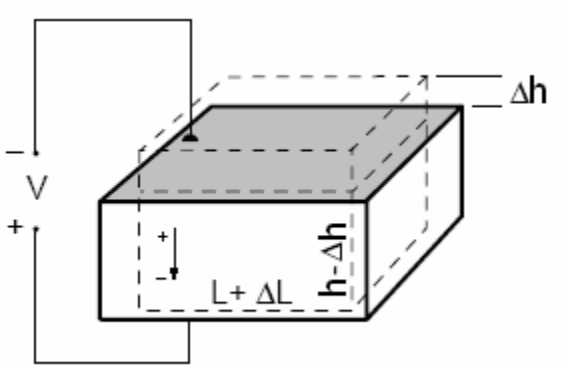

Figure 3.1.1: Change of dimension of a piezoelectric element when a voltage is applied (PIEZO SYSTEM, INC., 2005).

From **Figure 3.1.1** and equation (2.1.2), the length change can be expressed by

$$\frac{\Delta L}{L} = \frac{\Delta h}{h} = \frac{V d_{31}}{h} \tag{3.1.1}$$

where L is the length; h is the thickness; d_{31} is the piezoelectric strain constant; and V is the applied voltage. Therefore, the length change of piezoelectric materials is defined by

$$\Delta L = \frac{V\, d_{31}\, L}{h} \tag{3.1.2}$$

The two layers reduce drive voltage by half. Therefore, the length change of an actuator with two piezoelectric layers is defined by

$$\Delta L = 2\frac{V\, d_{31}\, L}{h} \tag{3.1.3}$$

Figure 3.1.2 shows the lateral motion of the system where d represents the displacement in the lateral direction.

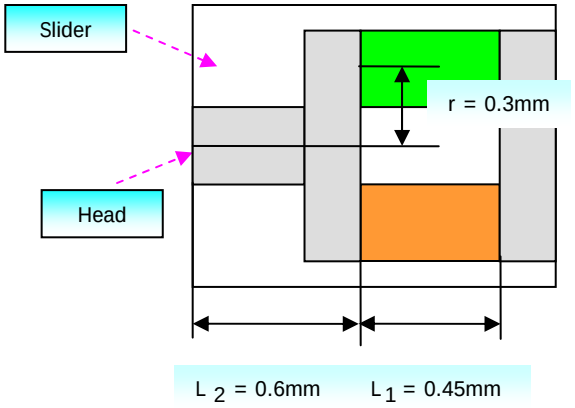

(a) No voltage

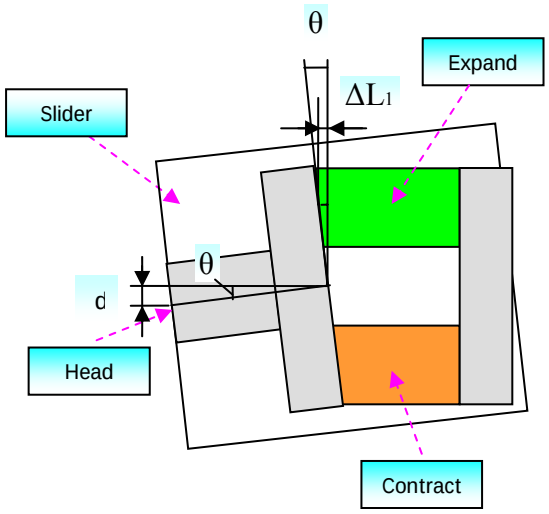

(b) A Voltage is applied

Figure 3.1.2: Lateral motion of the actuator system (top view).

In **Figure 3.1.2**, θ is very small, so d is defined by

$$d = L_2\theta \tag{3.1.4}$$

where L_2 is the length between the center of rotation and the head; θ is the rotational angle. The length change of an actuator is defined by

$$\Delta L_1 = r\theta \tag{3.1.5}$$

where r is the length of moment arm in the lateral direction; L_1 is the length of the lateral actuator. From equation (3.1.3), the change of length of piezoelectric actuator is also defined by

$$\Delta L_1 = 2\left|d_{31}\right|\frac{L_1}{h}V \tag{3.1.6}$$

where V is the applied voltage; h is the thickness of the single piezoelectric layer; and d_{31} is the piezoelectric strain constant. Substituting equation (3.1.6) into (3.1.5) yields θ defined by

$$\theta = \frac{2}{r}\left|d_{31}\right|\frac{L_1}{h}V \tag{3.1.7}$$

Substituting equation (3.1.7) into (3.1.4) gives the lateral displacement d defined by

$$d = L_2\frac{2}{r}\left|d_{31}\right|\frac{L_1}{h}V \tag{3.1.8}$$

Figure 3.1.3 shows an increase in displacement as applied voltage is increased.

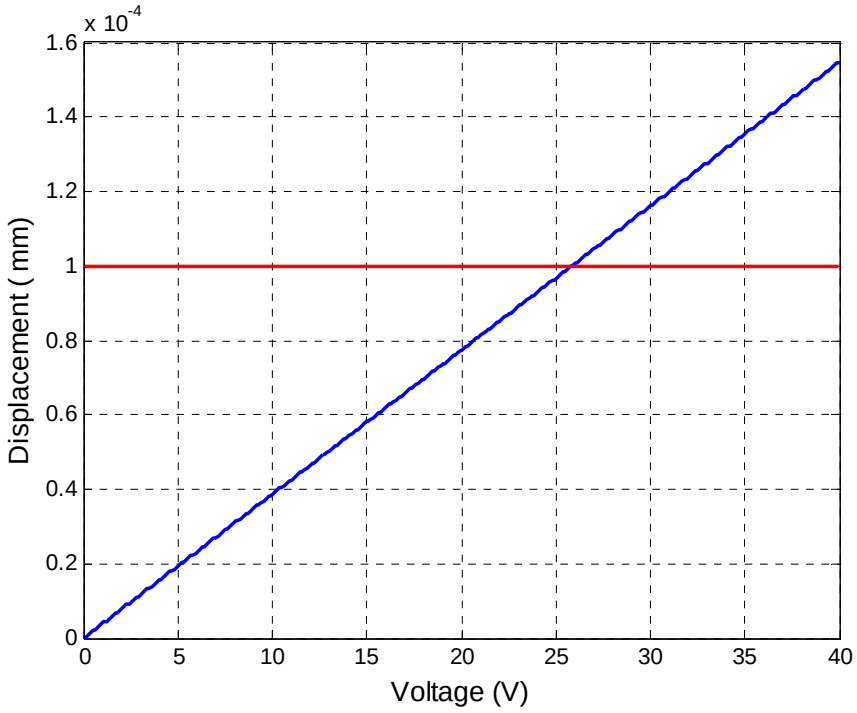

Figure 3.1.3: Lateral displacement of piezoelectric actuator.

To satisfy the target performance given in Chapter Two, the actuator should generate the displacement more than $0.1\mu m$, which corresponds to the half of the maximum stroke of the displacement. Therefore, the maximum voltage is set to 30V.

3.1.2 Dynamic system equation of the lateral actuator

The dynamic equation of motion of the lateral actuator is derived in this section. **Figure 3.1.4** shows the schematic drawing of the actuator system. The piezoelectric element is considered as the mass and spring system.

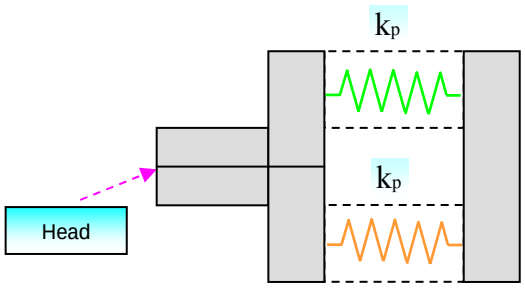

(a) No voltage

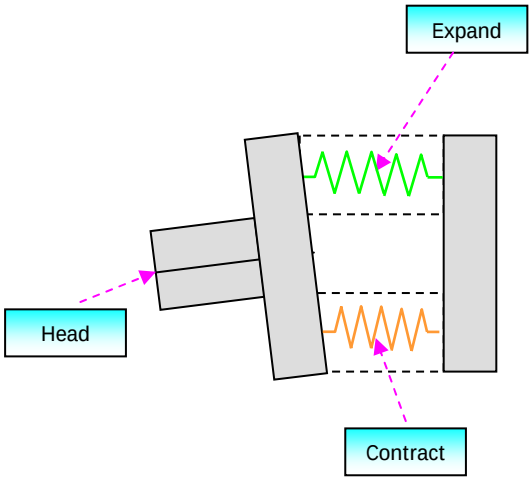

(b) A voltage is applied

Figure 3.1.4: Equivalent mass and spring system of the lateral actuator.

where k_p is the equivalent spring constant of the single piezoelectric layer defined by

$$k_p = \frac{A_c Y_p}{L_1}. \tag{3.1.9}$$

where Y_p is Young's modulus of piezoelectric materials; A_c is the cross section area of the single piezoelectric layer; and L_1 is the length of the lateral actuator. The free body diagram of the lateral actuator system is shown in **Figure 3.1.5**.

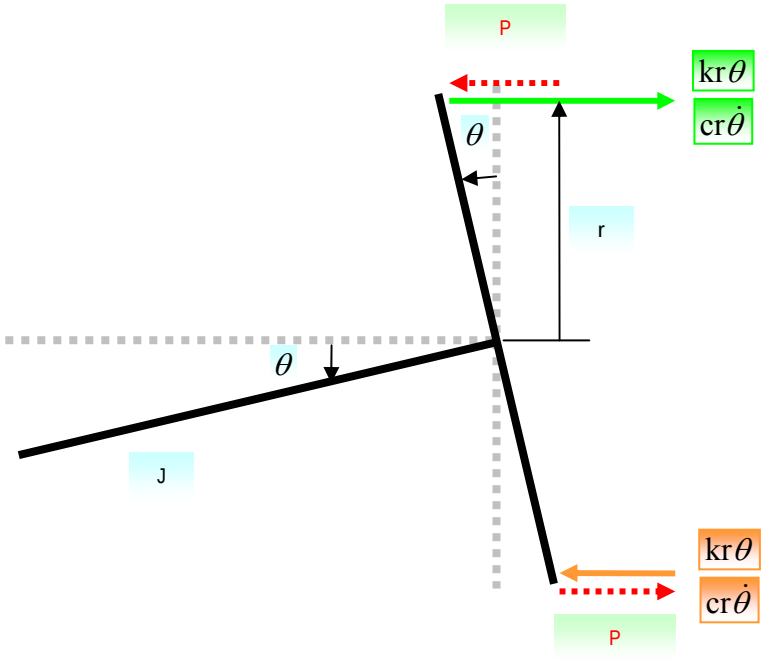

Figure 3.1.5: Free body diagram of the lateral actuator system.

where k is the spring constant of the system; c is the damping constant of the system; J is

the mass moment of inertia of the system; P is the input force generated by an applied voltage. From **Figure 3.1.5**, the system equation can be defined by

$$J\ddot{\theta} = -2cr^2\dot{\theta} - 2kr^2\theta + 2Pr \qquad (3.1.10\text{-a})$$

$$J\ddot{\theta} + 2cr^2\dot{\theta} + 2kr^2\theta = 2Pr \qquad (3.1.10\text{-b})$$

Substituting equation (3.1.4) into equation (3.1.10-b) yields

$$J\ddot{d} + 2cr^2\dot{d} + 2kr^2 d = 2L_2 Pr \qquad (3.1.11)$$

Since the actuator has two layers, k is defined by

$$k = 2k_p \qquad (3.1.12)$$

where k_p is the equivalent spring constant of the single piezoelectric layer and the input force P is defined by

$$P = 2P_p \qquad (3.1.13)$$

where P_p is the force generated by the single piezoelectric layer. **Figure 3.1.6** shows the lateral piezoelectric microactuator.

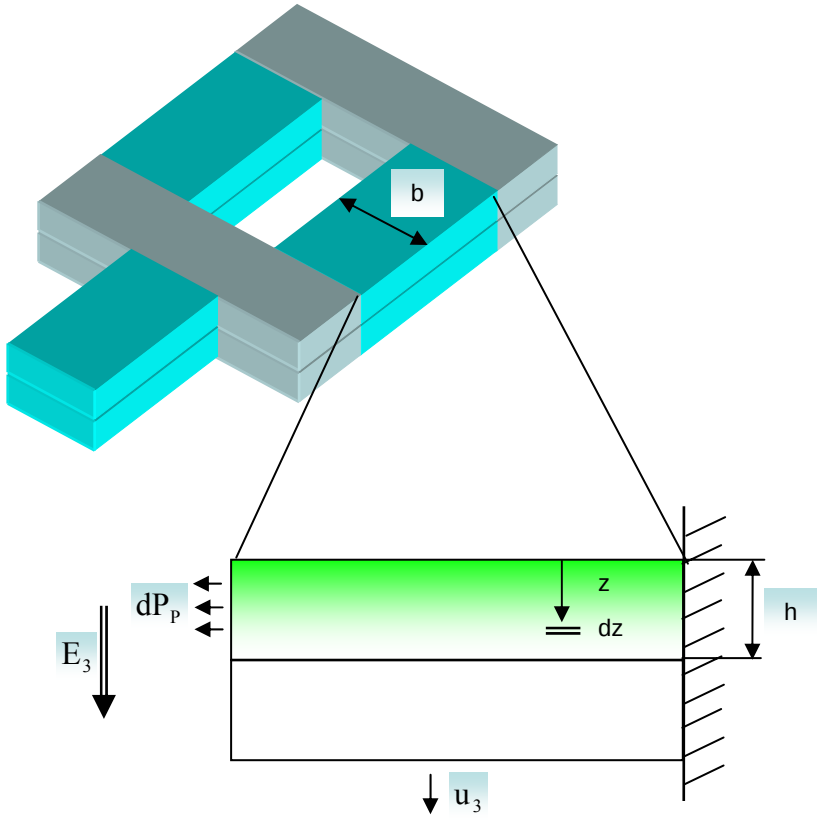

Figure 3.1.6: Lateral piezoelectric microactuator (side view).

A strain multiplied by a cross-section area (bh) gives an equivalent force, so force dP_p can be calculated by

$$dP_p = b\, e_{31}\, E_3\, dz \tag{3.1.14}$$

where b is the actuator width; e_{31} is the piezoelectric stress coefficient; E_3 is the electric field. In the beam case, the piezoelectric stress coefficient is defined by

$$e_{31} = Y_p \, d_{31} \tag{3.1.15}$$

where d_{31} is the piezoelectric strain coefficient; Y_p is Young's modulus of piezoelectric materials. Substituting equation (3.1.15) into equation (3.1.14) yields

$$dP_p = bY_p \, d_{31} E_3 dz \tag{3.1.16}$$

Integrating both sides of equation (3.1.16) with respect to z gives P_p defined as

$$P_p = \int_0^h bY_p \, d_{31} E_3 dz \tag{3.1.17-a}$$

$$= Y_p \, d_{31} E_3 bh \tag{3.1.17-b}$$

For a uniformly distributed electric field, E_3 is defined by

$$E_3 = \frac{V}{2h} \tag{3.1.18}$$

Substituting equation (3.1.18) into equation (3.1.17-b) gives P_p defined as

$$P_p = \frac{Y_p \, d_{31} \, b \, V}{2} \tag{3.1.19}$$

Let the input voltage V be defined by

$$V = V_0 \sin\omega t \tag{3.1.20}$$

where V_0 is the input amplitude and ω is the input frequency. Substituting equation (3.1.13), (3.1.19) and (3.1.20) into equation (3.1.11) yields the dynamic equation of

motion defined as

$$J\ddot{d} + 2cr^2\dot{d} + 2kr^2 d = 2\,r\,L_2 Y_p\,d_{31} b\,V_0 \sin\omega t \qquad (3.1.21\text{-a})$$

$$\ddot{d} + \frac{2cr^2}{J}\dot{d} + \frac{2kr^2}{J}d = \frac{2\,r\,L_2 Y_p\,d_{31}\,b\,V_0}{J}\sin\omega t \qquad (3.1.21\text{-b})$$

If we define the natural frequency is

$$\omega_n = \sqrt{\frac{2kr^2}{J}} \qquad (3.1.22)$$

,the damping ratio is

$$\zeta = \frac{cr^2}{J\omega_n} \qquad (3.1.23)$$

and the amplitude is

$$F_0 = 2\,r\,L_2 Y_p\,d_{31}\,b\,V_0 \qquad (3.1.24)$$

, then equation (3.1.21-b) becomes

$$\ddot{d} + 2\zeta\omega_n\dot{d} + \omega_n{}^2 d = \frac{F_0}{J}\sin\omega t \qquad (3.1.25)$$

3.1.3 System parameters of the lateral actuator system

System parameters of the system are evaluated in this section.

Natural frequency

From equation (3.1.9), (3.1.12), and (3.1.22), the natural frequency is defined by

$$\omega_n = \sqrt{\frac{4A_c Y_p r^2}{J L_1}} = 2.0941 \times 10^6 \tag{3.1.26}$$

Where Y_p is Young's modulus of piezoelectric materials; A_c is the cross section area of the single piezoelectric layer; L_1 is the length of the lateral actuator; J is the mass moment of inertia of the system; and r is the length of arm in lateral direction.

Mass moment of inertia

Figure 3.1.7 (a) shows how the slider and the actuator move when a voltage is applied. Let P_c be the center of rotation of the body, and the actuator and the slider rotate about the line through point P_c when a voltage is applied.

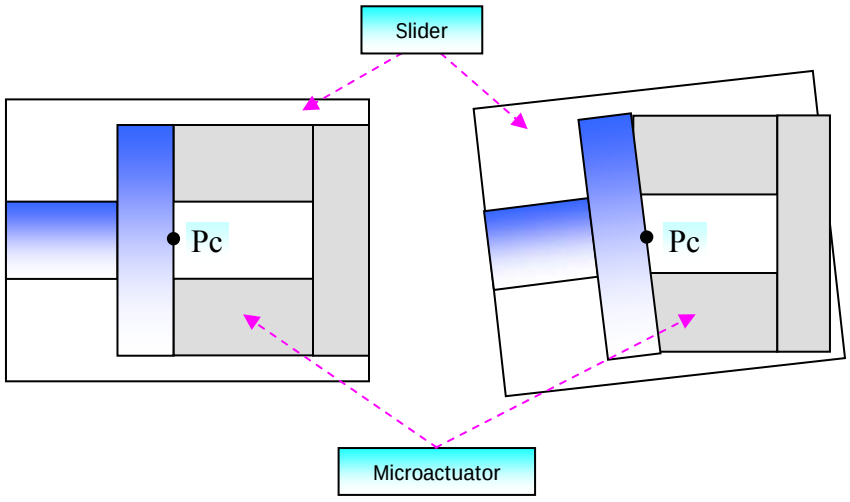

(a) Top View

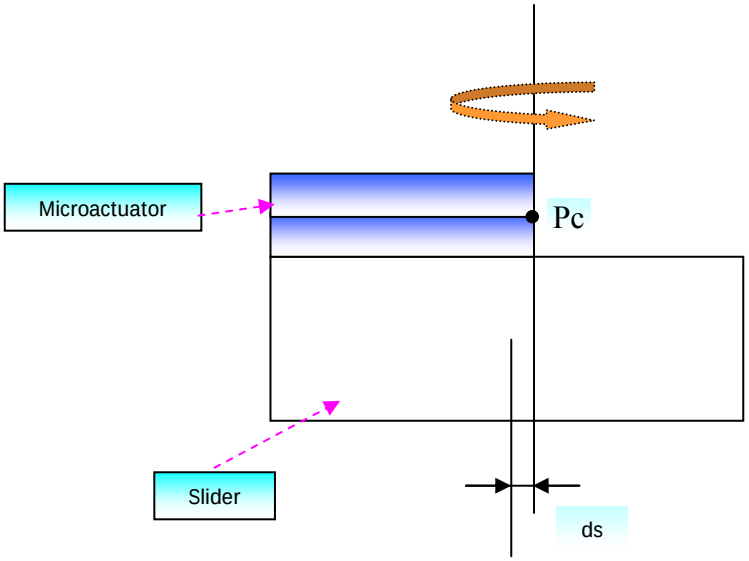

(b) Side View

Figure 3.1.7: Rotation of the slider and the actuator when a voltage is applied.

Because the mass of the piezoelectric materials is very small as compared with the slider, the effect of the mass of the piezoelectric materials is ignored. The mass moment of inertia of the slider about the line through point P_c is defined by

$$\begin{aligned} J &= J_c + d_s{}^2 m_s \\ &= 3.67 \times 10^{-7}\,\mathrm{kg \cdot mm^2} \end{aligned} \tag{3.1.27}$$

where J_c is moment of inertia about the center of mass; d_s is distance between the center of mass of the slider and the axis through the point P_c (0.125mm); and m_s is the slider mass (1.6mg).

Damping ratio

The damping of the system is related to the heat generation of piezoelectric materials, system frictions and so on. Based on the study of piezoelectric actuators for high storage density hard disk drives, a 0.5 % damping is assumed in this study. Further experimental work for evaluating the damping of the proposed actuator system is desirable. A variety of system responses with different damping ratios will be evaluated in Chapter Four.

3.2 System Equation of the Transverse Actuator

In this section, the maximum input voltage that ensures the target performance in the transverse direction is calculated first. The generic dynamic system equation of the transverse actuator system is defined, followed by the dynamic system equation in specific conditions (in the first mode and at the free end of the bimorph actuator beam). Finally, the system parameters are evaluated. Since the slider is free at the boundary, it is assumed that the deflection of the slider is identical to the deflection of the piezoelectric actuator.

3.2.1 Maximum input voltage for the traverse actuator

Based on the target displacement which is given in Chapter Two, the required maximum input voltage for target flying height is calculated. **Figure 3.2.1** shows the transverse motion of the system where d represents the deflection in the transverse direction.

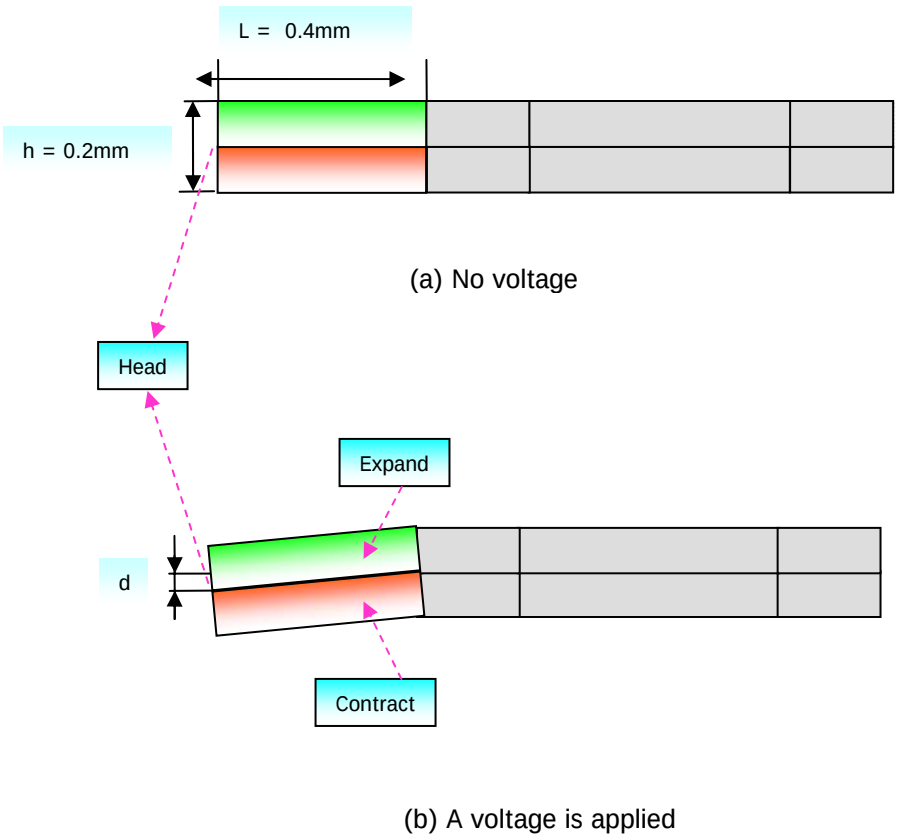

Figure 3.2.1: Transversal motion of the actuator system (side view).

Figure 3.2.2 shows the schematic diagram of the transverse actuator.

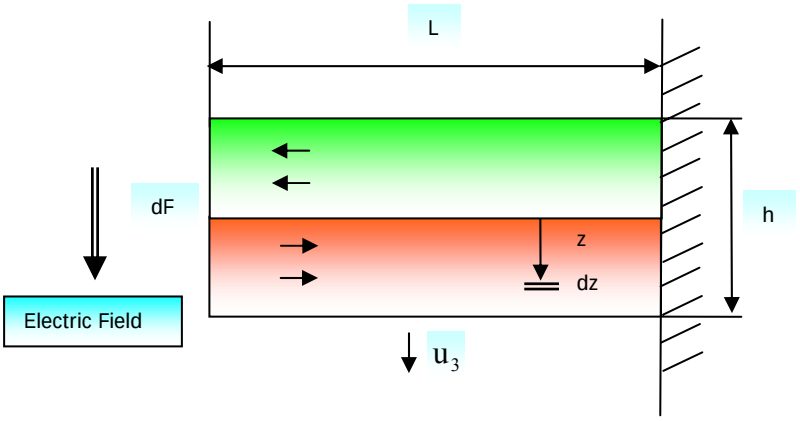

Figure 3.2.2: Transverse piezoelectric actuator (side view).

From equation (3.1.16), force dF can be calculated from strains and cross section area.

$$dF = bY_p d_{31} E_3 dz \tag{3.2.1}$$

Force multiplied by a moment arm z yields a bending moment.

$$dM = bY_p d_{31} E_3 z dz \tag{3.2.2}$$

Thus, the bending moment M with respect to the neutral axis is defined by

$$M = \int_{-\frac{h}{2}}^{\frac{h}{2}} bY_p d_{31} E_3 z dz \tag{3.2.3-a}$$

$$= Y_p d_{31} E_3 \frac{bh^2}{4} \tag{3.2.3-b}$$

For a uniformly distributed electric field, E_3 is defined by

$$E_3 = \frac{V}{h} \tag{3.2.4}$$

Substituting equation (3.2.4) into equation (3.2.3-b) gives the bending moment M defined by

$$M = Y_p d_{31} V \frac{bh}{4} \tag{3.2.5}$$

The moment also can be defined by

$$M = Y_p I \left(\frac{\partial^2 u_3}{\partial x^2} \right) \tag{3.2.6}$$

where I is the area moment of inertia $\left(I = \frac{bh^3}{12} \right)$; Y_p is Young's modulus of piezoelectric materials. From equation (3.2.5) and (3.2.6),

$$Y_p I \left(\frac{\partial^2 u_3}{\partial x^2} \right) = Y_p d_{31} V \frac{bh}{4} \tag{3.2.7}$$

Integrating both sides of equation (3.2.7) with respect to x gives the displacement $u_3(x)$ as

$$u_3(x) = \frac{3d_{31}V}{2h^2}x^2 + c_1x + c_2 \tag{3.2.8}$$

From the boundary conditions of the beam (at the fixed end): $u_3(0) = 0$; and $\frac{\partial u_3(0)}{\partial x} = 0$, $c_1 = 0$; and $c_2 = 0$. Therefore, equation (3.2.8) becomes

$$u_3(x) = \frac{3d_{31}V}{2h^2}x^2 \tag{3.2.9}$$

Since the maximum deflection of the beam occurs at the end of the beam, the deflection of the bimorph actuator at the end of the beam is defined by

$$d = \frac{3}{2}\left(\frac{L}{h}\right)^2 |d_{31}|V \tag{3.2.10}$$

where L is the length of the beam; h is the thickness of the beam; V is the applied voltage; and d_{31} is the piezoelectric strain constant. As mentioned in Chapter One, currently the flying height of sliders is 20-25nm without any height adjusting actuator in 3.5" drives. By considering the currently achieved flying height and the deflection of the bimorph actuator, we can calculate the flying height of the system with the microactuator. **Figure 3.2.3** shows achieved flying height at different applied voltage.

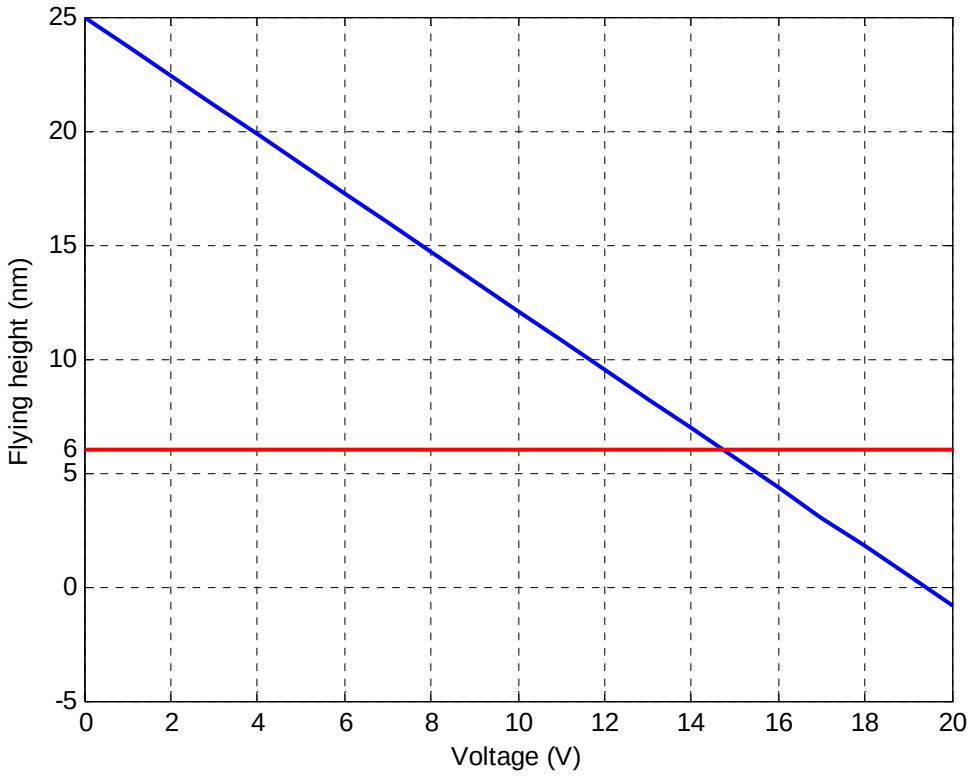

Figure 3.2.3: Flying height of piezoelectric actuator.

To satisfy the target requirement which is given in Chapter Two, the flying height should be less than 6nm. Therefore, the maximum voltage is set to 16V.

3.2.2 Dynamic system equation of the transverse actuator

The dynamic equation of the transverse actuator is derived in this section. **Figure 3.2.4** shows the schematic diagram of the piezoelectric bimorph actuator which regulated the

transverse motion of the system. The generic dynamic system equation of the actuator system is defined next.

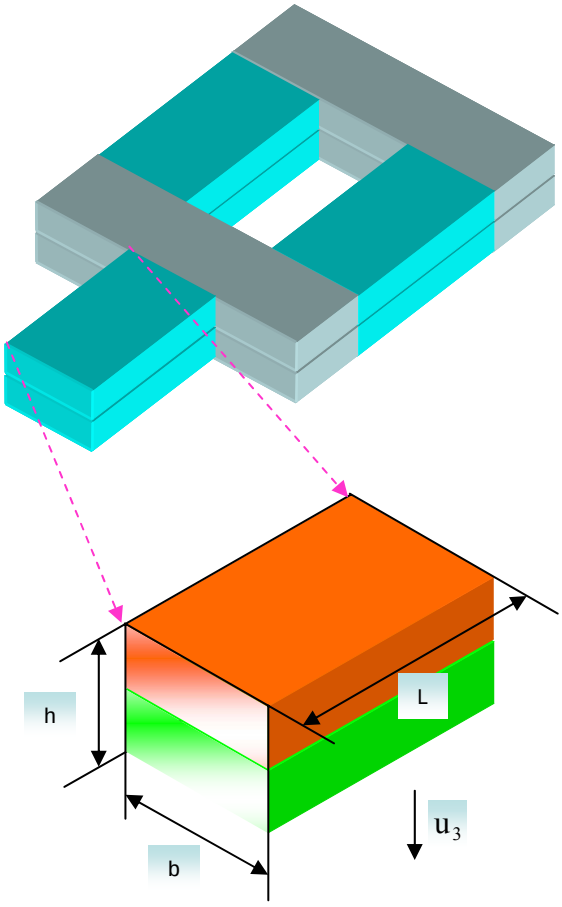

Figure 3.2.4: Transverse piezoelectric bimorph actuator.

The system equation of the beam in the transverse direction is derived as

$$D\frac{\partial^4 u_3}{\partial x^4} + \rho h\ddot{u}_3 = q_3 \tag{3.2.11}$$

where ρ is the mass density; h is the beam thickness; D is the bending stiffness $\left(D = \frac{Yh^3}{12(1-\mu^2)}\right)$; q_3 is the control force induced by external applied voltages; Y is Young's modulus; and μ is Poisson's ratio. Since the beam has a rectangular cross section and Poisson's ratio is neglected in a beam case, so the system equation of the beam becomes

$$YI\frac{\partial^4 u_3}{\partial x^4} + b\,\rho h\ddot{u}_3 = bq_3 \tag{3.2.12}$$

where I is the area moment of inertia $\left(I = \frac{bh^3}{12}\right)$. Let $\rho' = b\,\rho t$, $q_3' = bq_3$, then equation (3.2.12) becomes

$$YI\frac{\partial^4 u_3}{\partial x^4} + \rho'\ddot{u}_3 = q_3' \tag{3.2.13}$$

The modal expansion concept implies that the total response of a generic shell continuum is composed of all participating modes. Thus, the solution of equation (3.2.13) is defined by

$$u_3 = \sum_{m=1}^{\infty} \eta_m(t) \cdot U_{3m}(x) \tag{3.2.14}$$

where η_m is the modal participation factor; $U_{3m}(x)$ is the mode shape function; and the

subscripts m denote the m-th mode. The modal participation factor η_m is satisfied by the following equation.

$$\ddot{\eta}_m + \frac{c_m}{\rho h}\dot{\eta}_m + \omega_m{}^2\eta_m = F_m \tag{3.2.15}$$

where ω_m is the natural frequency; c_m is the modal damping; F_m is the modal force, which is defined by

$$F_m = \frac{1}{\rho h N_m}\int_o^L q_3 U_{3m} dx \tag{3.2.16}$$

and N_m is defined by

$$N_m = \int_o^L \left(U_{3m}\right)^2 dx \tag{3.2.17}$$

If we define the modal damping ratio ζ_m as

$$\zeta_m = \frac{c_m}{2\rho\, h\omega_m} \tag{3.2.18}$$

,then equation (3.2.15) becomes

$$\ddot{\eta}_m + 2\zeta_m\omega_m\dot{\eta}_m + \omega_m{}^2\eta_m = F_m \tag{3.2.19}$$

The mode shape function $U_{3m}(x)$ of a cantilever beam is defined by

$$U_{3m}(x) = \left(C(\lambda_m x) - \frac{A(\lambda_m L)}{B(\lambda_m L)}D(\lambda_m x)\right) \tag{3.2.20}$$

where the coefficients are

$$A(\lambda_m x) = 0.5\left[\cosh(\lambda_m x) + \cos(\lambda_m x)\right] \tag{3.2.21}$$

$$B(\lambda_m x) = 0.5\left[\sinh(\lambda_m x) + \sin(\lambda_m x)\right] \tag{3.2.22}$$

$$C(\lambda_m x) = 0.5\left[\cosh(\lambda_m x) - \cos(\lambda_m x)\right] \tag{3.2.23}$$

$$D(\lambda_m x) = 0.5\left[\sinh(\lambda_m x) - \sin(\lambda_m x)\right] \tag{3.2.24}$$

where x defines the distance measured from the fixed end. The eigenvalue λ_m is determined form its characteristic equation defined by

$$\cosh(\lambda_m L)\cos(\lambda_m L) + 1 = 0 \tag{3.2.25}$$

Equation (3.2.25) gives

$$\lambda_1 L = 1.875 \tag{3.2.26}$$

$$\lambda_2 L = 4.694 \tag{3.2.27}$$

$$\lambda_3 L = 7.855 \tag{3.2.28}$$

$$\lambda_4 L = 10.996 \tag{3.2.29}$$

$$\lambda_5 L = 14.137 \tag{3.2.30}$$

The natural frequency is defined by

$$\omega_m = \sqrt{\frac{YI}{\rho'}}(\lambda_m)^2 \tag{3.2.31}$$

Since the first mode resonance frequency limits the expansion of operation bandwidth, the dynamic system equation of the system for only the first mode is considered in this study. The bending motion is generated by strains in the piezoelectric actuator when a voltage is applied. An input voltage is a uniformly distributed sinusoidal surface loading (in V). This voltage input (in V) can be transformed into an equivalent distributed loading p_3 (in N). The equivalent distributed loading p_3 should generate the same deflection at the free end of the bimorph beam as the resulting from an applied voltage shown as **Figure 3.2.5**.

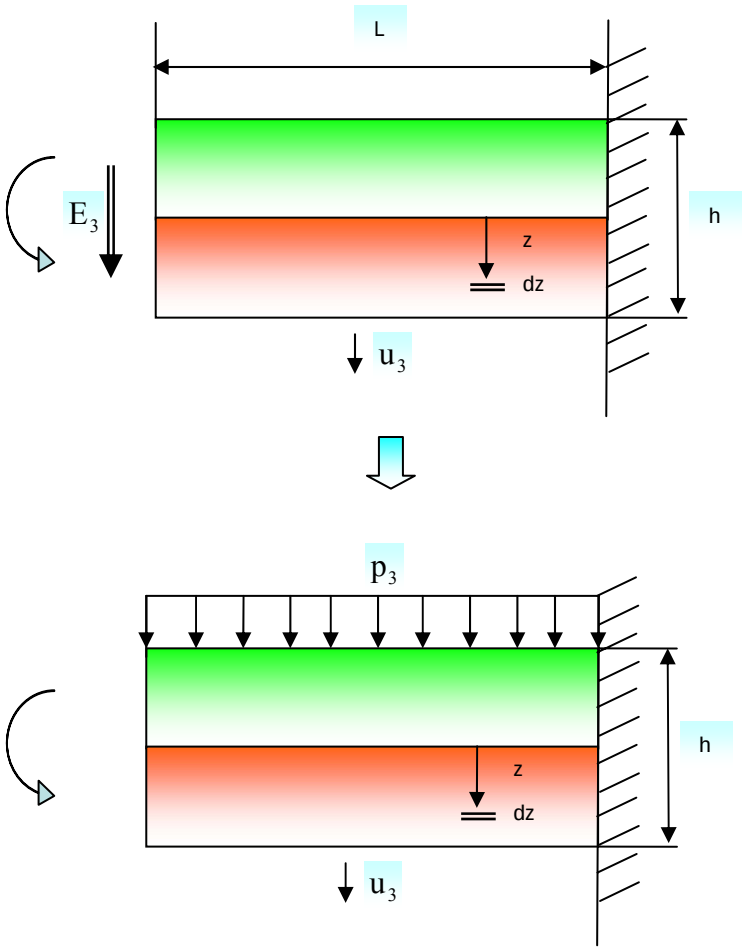

Figure 3.2.5: Voltage input and equivalent distributed loading.

The load-deflection beam equation is defined by

$$YIu_3''''(x) = p_3 \tag{3.2.32}$$

The boundary conditions of the cantilever beam are defined by

$$\begin{aligned} &\text{Free end} : \quad x = L \quad u_3'' = 0; \quad u_3''' = 0 \\ &\text{Fixed end} : \quad x = 0 \quad u_3 = 0; \quad u_3' = 0 \end{aligned} \tag{3.2.33}$$

Integrating four times both sides of equation (3.2.32) with respect to x yields

$$YIu_3(x) = \frac{p_3}{24}x^4 + \frac{c_1}{6}x^3 + \frac{c_2}{2}x^2 + c_3x + c_4 \tag{3.2.34}$$

From the B.C in equation (3.2.33), $c_1 = -p_3 L$, $c_2 = \frac{1}{2}p_3 L^2$, $c_3 = 0$, and $c_4 = 0$.

Therefore, the equation (3.2.34) becomes

$$YIu_3(x) = \frac{p_3}{24}x^4 - \frac{p_3}{6}Lx^3 + \frac{p_3}{4}L^2x^2 \tag{3.2.35}$$

Therefore, the deflection of the end of beam (x = L) is defined by

$$u_3(L) = \frac{p_3}{8YI}L^4 \tag{3.2.36}$$

The deflection from equation (3.2.36) is same as the deflection from equation (3.2.10). Therefore,

$$\frac{3}{2}\left(\frac{L}{h}\right)^2 d_{31}V = \frac{p_3}{8YI}L^4 \tag{3.2.37}$$

Therefore, the distributed force p_3 is defined by

$$p_3 = \frac{12Y\,I\,d_{31}}{h^2L^2}V \tag{3.2.38-a}$$

$$= \frac{Y\,d_{31}bh}{L^2}V \tag{3.2.38-b}$$

If we consider only the first mode, equation (3.2.14) becomes

$$u_3(x,t) = \eta_1(t) \cdot U_{31}(x) \tag{3.2.39}$$

From equation (3.2.19) and (3.2.39), the dynamic system equation in the first mode is defined by

$$\ddot{u}_3 + 2\zeta_1\omega_1\dot{u}_3 + \omega_1^2 u_3 = U_{31}(x)\, F_1^* \sin\omega t \tag{3.2.40}$$

At the free end of the beam (x = L), the dynamic system equation (3.2.40) becomes

$$\ddot{u}_3 + 2\zeta_1\omega_1\dot{u}_3 + \omega_1^2 u_3 = U_{31}(L)\, F_1^* \sin\omega t \tag{3.2.41}$$

where

$$F_1^* = \frac{1}{\rho h N_1}\int_o^L p_3 U_{31} dx \tag{3.2.42-a}$$

$$= \frac{Y\ d_{31}\ b\ h\ V_0}{L^2 \rho N_1}\int_o^L U_{31} dx \tag{3.2.42-b}$$

3.2.3 System parameters of the transverse actuator system

System parameters of the system in the first mode are calculated in this section.

Natural frequency

From equation (3.2.31), the natural frequency of the system in the first mode is defined by

$$\omega_1 = \sqrt{\frac{Y_p I}{\rho_p bh}} \lambda_1^{\ 2} = 1.2018 \times 10^5 \qquad (3.2.43)$$

Damping ratio

The damping of the system is related to the heat generation of piezoelectric materials, system frictions and so on. Based on the study of piezoelectric actuators for high storage density hard disk drives, a 0.5 % damping is assumed in this study. Further experimental work for evaluating the damping of the proposed actuator system is desirable. A variety of system responses with different damping ratios will be evaluated in Chapter Four. The dynamic system equations and system parameters of the piezoelectric microactuator system, which are defined in this chapter, will be used in the next chapters for frequency and time response analysis of the system.

Chapter Four
Frequency Response of the Actuator System

In this chapter, the frequency responses of the actuator system are presented. A Bode plot is used for displaying of the frequency response; MATLAB is used to calculate the frequency response of the actuator. Because the state-space method is well suited to the use of computer techniques, a state-space model is used in this chapter.

4.1 Frequency Response of the Actuator System in the Lateral Direction

In the lateral direction, the conventional voice coil motor (VCM) actuator is used at low frequency part and the piezoelectric microactuator is used at high frequency part to control the lateral movement. The frequency responses for VCM and the piezoelectric microactuator are presented in this section. In this thesis, the VCM model designed by Venkataramanan et al. (2002) [16] is used for the system frequency response analysis at low frequency part.

4.1.1 Characteristics of the conventional voice coil motor

In this section, the system frequency response of VCM is given. Since there are a lot of available VCM models, the model designed by Venkataramanan et al. (2002) [16] is used in this study. The Maxtor hard disk drive (HDD) (Model 51536U3) is used for the simulation in his paper. The frequency response of VCM can be obtained using a laser Doppler vibrometer (LDV) and a dynamic signal analyzer. The control input u is a voltage to a current amplifier for VCM and the measurement output y is the head position in tracks. The frequency response of a commercially available HDD servo system from u to y is shown in **Figure 4.1.1**.

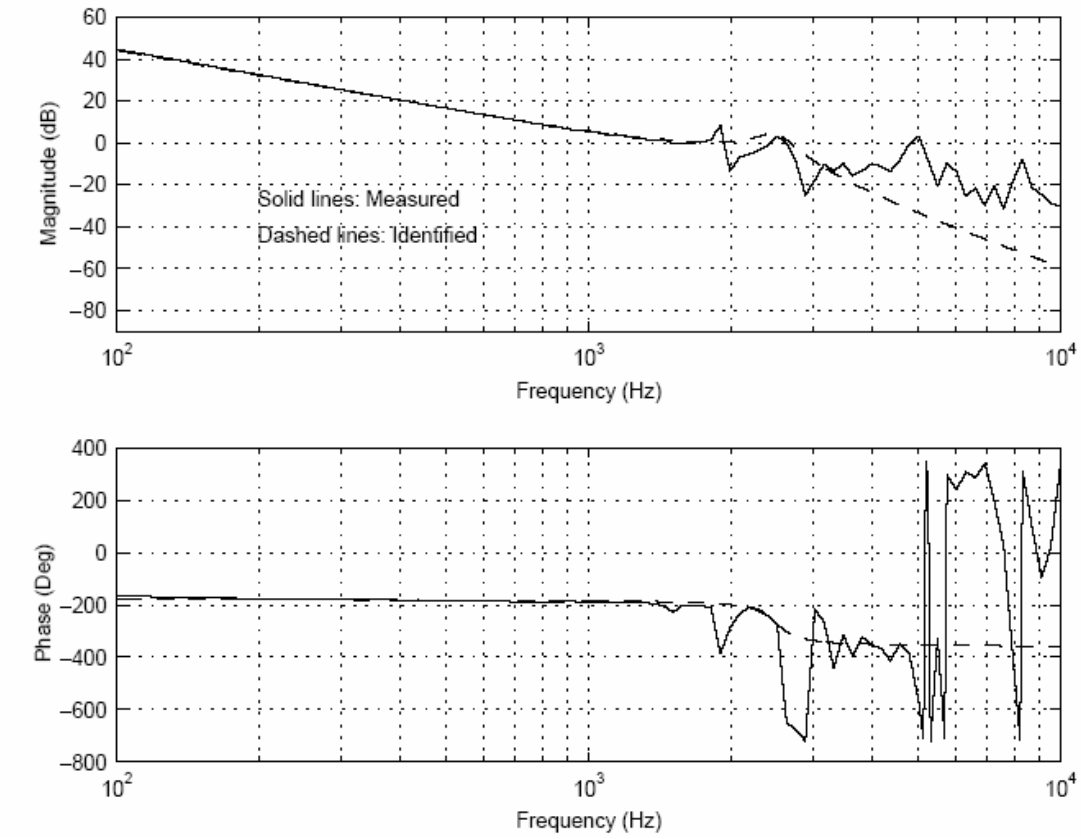

Figure 4.1.1: Frequency response of VCM (Venkataramanan et al., 2002) [16].

It is quite conventional to approximate the dynamics of the VCM actuator by a second-order state space model as

$$\dot{\mathbf{x}} = \mathbf{A}\mathbf{x} + \mathbf{B}\mathrm{u} = \begin{bmatrix} 0 & 1 \\ 0 & 0 \end{bmatrix}\mathbf{x} + \begin{bmatrix} 0 \\ \mathrm{a} \end{bmatrix}\mathrm{u} \tag{4.1.1}$$

$$\mathbf{x} = \begin{pmatrix} \mathrm{y} \\ \mathrm{v} \end{pmatrix} \tag{4.1.2}$$

where **x** is the state, which consists of the displacement y and the velocity v of the read/write head; u is the control input constrained by $|u(t)| \le u_{MAX}$ and a $a = \frac{K_t}{J_a}$ is the acceleration constant, with K_t being the torque constant and J_a being the moment of inertia of the actuator mass. Thus, the transfer function from u to y of the VCM model can be written as

$$G(s) = \frac{a}{s^2} \tag{4.1.3}$$

The bandwidth of such a system is typically limited to less than 1 kHz by the mechanical dynamics of VCM. The frequency response shows that the servo system has many mechanical resonance frequencies over 1 kHz. In general, the first mode limits the bandwidth. If only the first dominating resonance frequency is considered, a more realistic model for the VCM actuator should be given as (Venkataramanan et al., 2002) [16]

$$G(VCM) = \frac{6.4013 \times 10^7}{s^2} \times \frac{2.467 \times 10^8}{(s^2 + 2.513 \times 10^3 s + 2.467 \times 10^8)} \tag{4.1.4}$$

4.1.2 Characteristics of the lateral actuator

In this section, the system frequency response of the lateral piezoelectric microactuator is given, followed by discussion of target performance evaluation. Frequency responses of the actuator system with various system parameters are presented. This study can be used for future design improvement. From Chapter Three, equation (3.1.25), the system dynamic equation of lateral actuator is defined by

$$\ddot{d} + 2\zeta\omega_n \dot{d} + \omega_n{}^2 d = \frac{F_0}{J} \sin\omega t \tag{4.1.5}$$

The dynamic equation can be represented in the state-variable form with a control voltage input and a displacement output. Let $x_1 = d$, $x_2 = \dot{x}_1 = \dot{d}$, and a control input be u. The system equation (4.1.5) is expressed as matrix form which is defined by

$$\begin{bmatrix} \dot{x}_1 \\ \dot{x}_2 \end{bmatrix} = \begin{bmatrix} 0 & 1 \\ -\omega_n^{\,2} & -2\zeta\omega_n \end{bmatrix} \begin{bmatrix} x_1 \\ x_2 \end{bmatrix} + \begin{bmatrix} 0 \\ \dfrac{F_0}{J} \end{bmatrix} u \tag{4.1.6}$$

The output $y = x_1$ is the head position in the lateral direction. The system can be expressed by

$$\begin{aligned} \dot{\mathbf{x}} &= \mathbf{F}\mathbf{x} + \mathbf{G}u \\ y &= \mathbf{H}\mathbf{x} + Ju \end{aligned} \tag{4.1.7}$$

where $\mathbf{F}$ is the $n \times n$ system matrix defined by

$$\mathbf{F} = \begin{bmatrix} 0 & 1 \\ -\omega_n^{\,2} & -2\zeta\omega_n \end{bmatrix} \tag{4.1.8}$$

, $\mathbf{G}$ is the $n \times 1$ input matrix defined by

$$\mathbf{G} = \begin{bmatrix} 0 \\ \dfrac{F_0}{J} \end{bmatrix} \tag{4.1.9}$$

, $\mathbf{H}$ is the $1 \times n$ output matrix defined by

$$\mathbf{H} = \begin{bmatrix} 1 & 0 \end{bmatrix} \tag{4.1.10}$$

and J is the direct transmission term defined by

$$J = 0 \tag{4.1.11}$$

The transfer function of the lateral actuator with a control voltage input and a displacement output is obtained by using MATLAB.

$$G_{\text{pzt}} = \frac{-6.985\times10^{-10}\,\text{s} + 1.273\times10^{8}}{\text{s}^2 + 2.094\times10^{6}\,\text{s} + 4.385\times10^{12}} \tag{4.1.12}$$

Figure 4.1.2 and **Figure 4.1.3** show the frequency response of the lateral actuator. Bode plot is used for displaying of frequency response of the system. The idea in Bode's method is to plot magnitude curves using a logarithmic scale and phase curves using a linear scale.

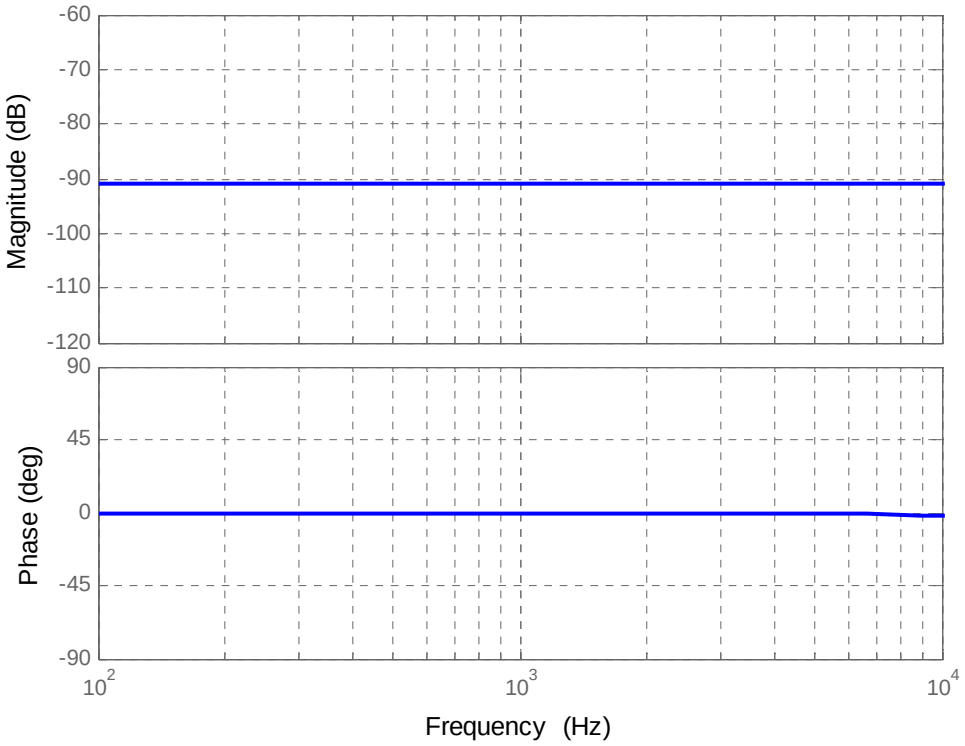

Figure 4.1.2: Frequency response of the lateral actuator (100 Hz-10 kHz).

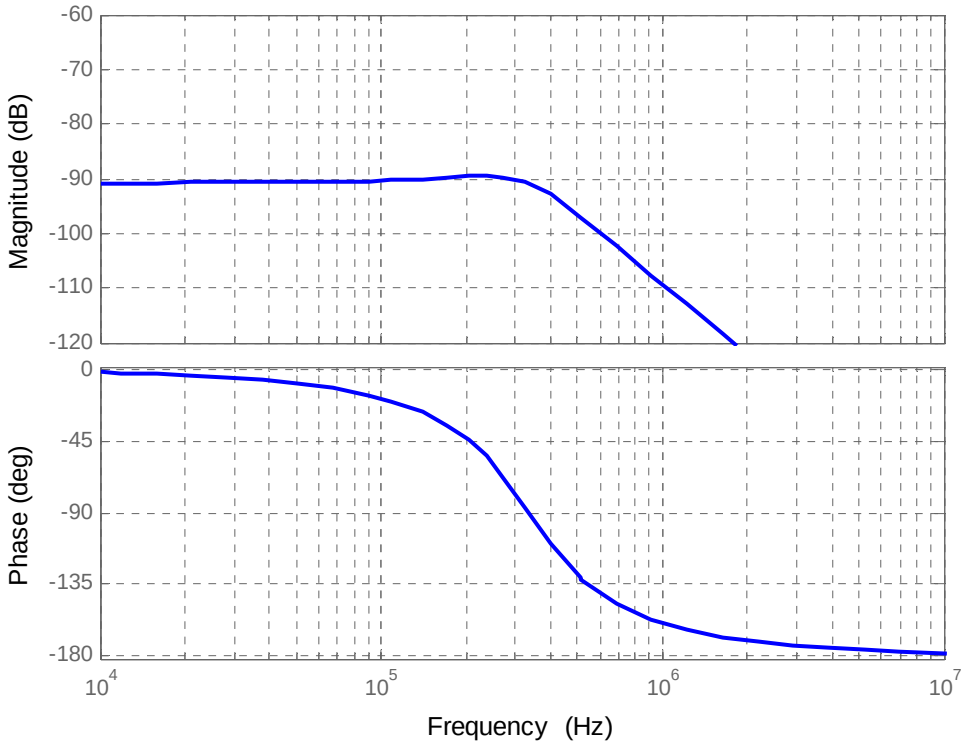

Figure 4.1.3: Frequency response of the lateral actuator (10 kHz-10MHz).

Comparing **Figure 4.1.2** and **Figure 4.1.3** to **Figure 4.1.1** shows that the microactuator is increasing the servo bandwidth. In Chapter Two, **Table 2.2.1,** the target bandwidth and resonance frequency were set to 5-6 kHz and 60 kHz respectively. The frequency response shows that the proposed piezoelectric actuator achieved servo bandwidth of more than 6 kHz under the 0.5 % damping assumption which is satisfies the target requirements.

4.1.3 Frequency response of the lateral actuator with a variety of system parameters

The current trend in hard disk design is towards smaller hard disks with increasingly larger capacities. Understanding how system parameters affect the performance of the actuator system is helpful to improve the design of actuators. For this purpose, the frequency responses of the system with a variety of system parameters are presented in this section.

Damping ratio

The effect of the damping ratio to the lateral actuator system is obtained. **Figure 4.1.4** and **Figure 4.1.5** show the system frequency response of the lateral actuator with different values of the damping ratio.

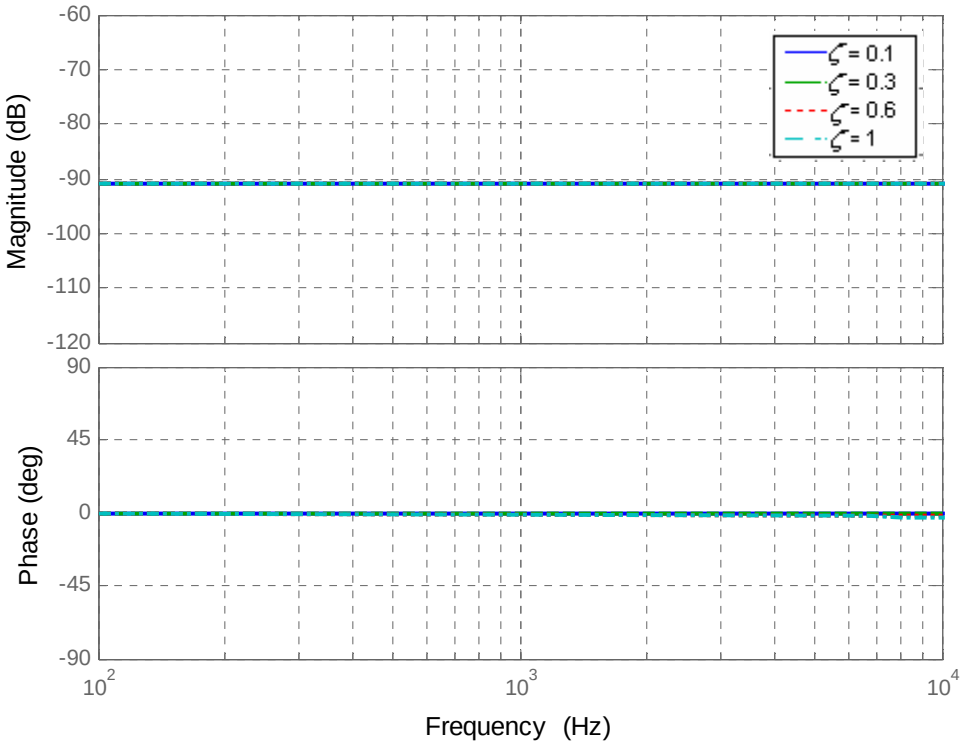

Figure 4.1.4: Frequency response of the lateral actuator at a variety of ζ values (100 Hz-10 kHz).

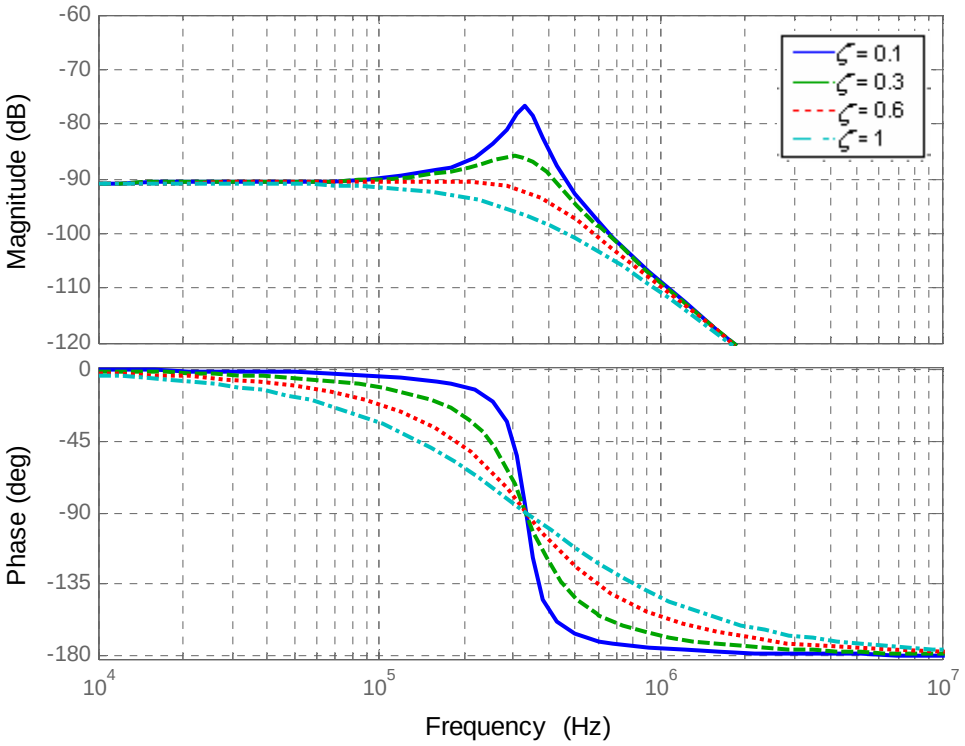

Figure 4.1.5: Frequency response of the lateral actuator at a variety of ζ values (10 kHz-10 MHz).

In the proposed actuator system, the damping ratio was assumed as $\zeta = 0.5$. The value of the damping ratio is changed from 0.1 to 1. **Figure 4.1.4** and **Figure 4.1.5** shows that the damping ratio ζ does not affect the mechanical resonant frequency of the system. However, damping has a large influence on the amplitude and phase angle in the frequency region near resonance. If the damping ratio is decreasing, the servo bandwidth is increasing. Decreasing the damping ratio is required to achieve high servo bandwidth.

Natural frequency

The effect of the natural frequency to the actuator system is obtained. **Figure 4.1.6** and **Figure 4.1.7** show the system frequency response of the lateral actuator with different values of natural frequency.

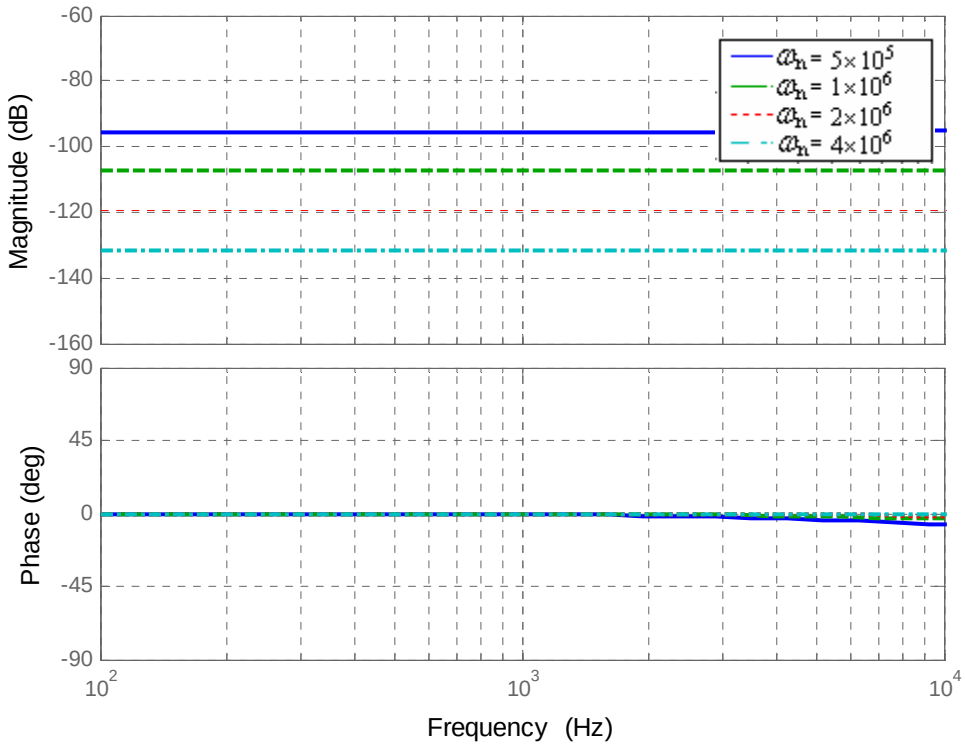

Figure 4.1.6: Frequency response of the lateral actuator at a variety of ω_n values (100 Hz-10 kHz).

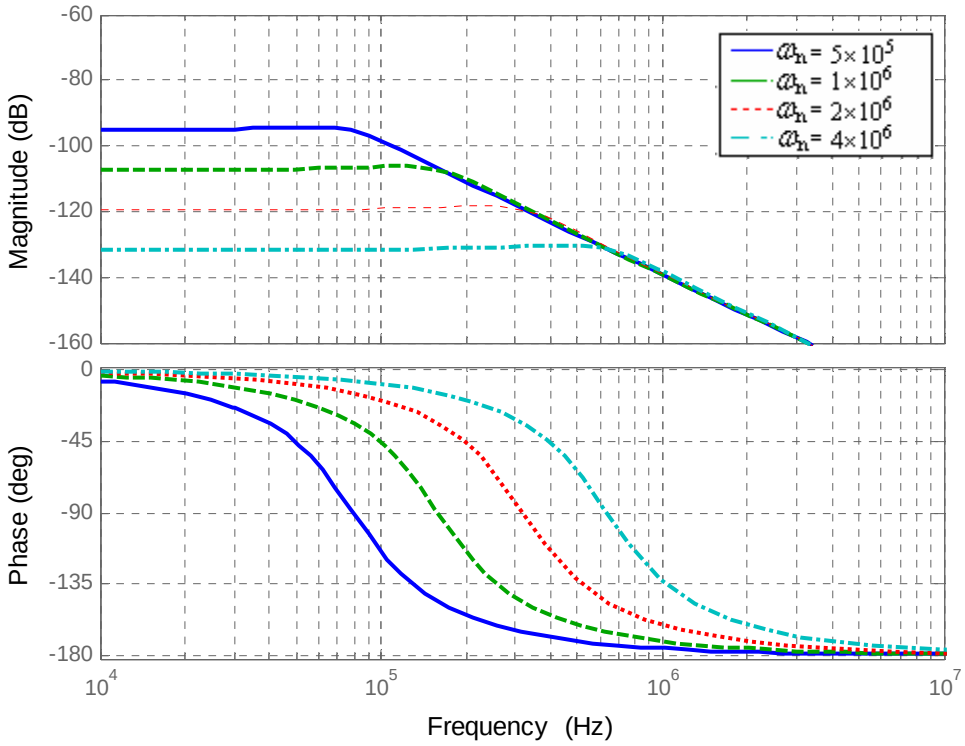

Figure 4.1.7: Frequency response of the lateral actuator at a variety of ω_n values (10 kHz-10 MHz).

In the proposed actuator system, the natural frequency $\omega_n = 2.0941\times10^6$. The value of the natural frequency is changed from 5×10^5 to 4×10^6. **Figure 4.1.6** and **Figure 4.1.7** show that if the natural frequency is increasing, the servo bandwidth and resonance frequency are also increasing. Increasing the natural frequency is required to achieve better performance of the actuator system. In the Chapter Three, equation (3.1.26), the natural frequency is defined by

$$\omega_n = \sqrt{\frac{4A_c Y_p r^2}{J L_1}} \tag{4.1.13}$$

To increase the natural frequency, increasing the cross section area or the length of arm of the lateral actuator, choosing a piezoelectric material with larger Young's modulus, or reducing the length or mass moment of inertia of the lateral actuator are needed. Since these variables are also related with the lateral displacement, size and shape of the actuator, changing these values should be considered carefully.

Mass moment of inertia

The effect of the rotational mass moment of inertia to the actuator system is obtained. **Figure 4.1.8** and **Figure 4.1.9** show the system frequency response of the lateral actuator with different values of the rotational moment of inertia.

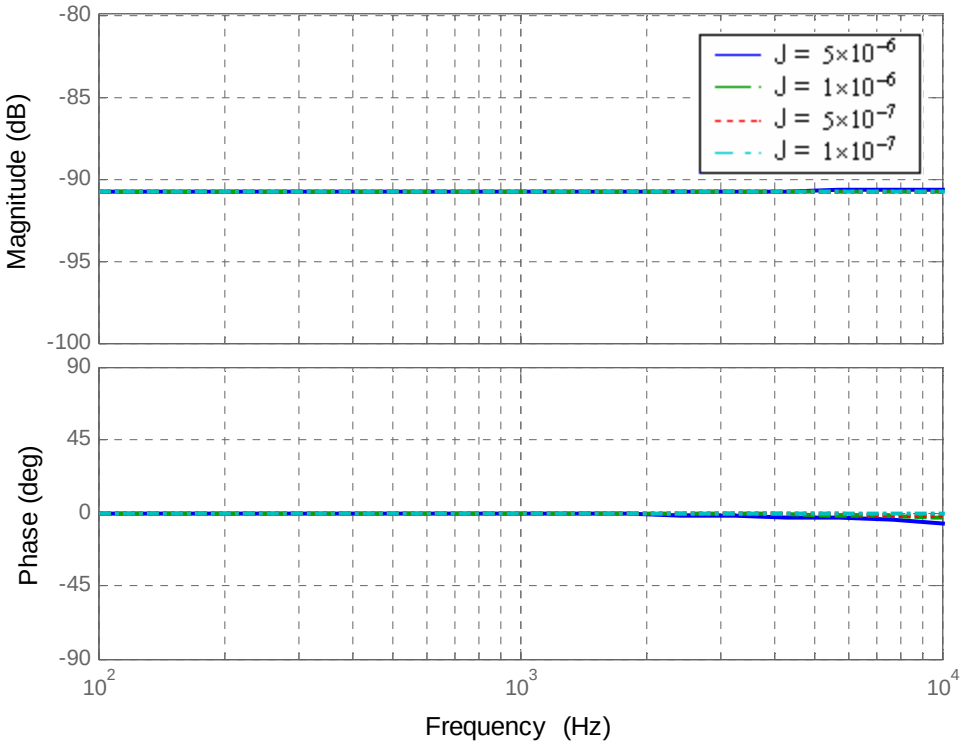

Figure 4.1.8: Frequency response of lateral actuator at a variety of J values (100 Hz-10 kHz).

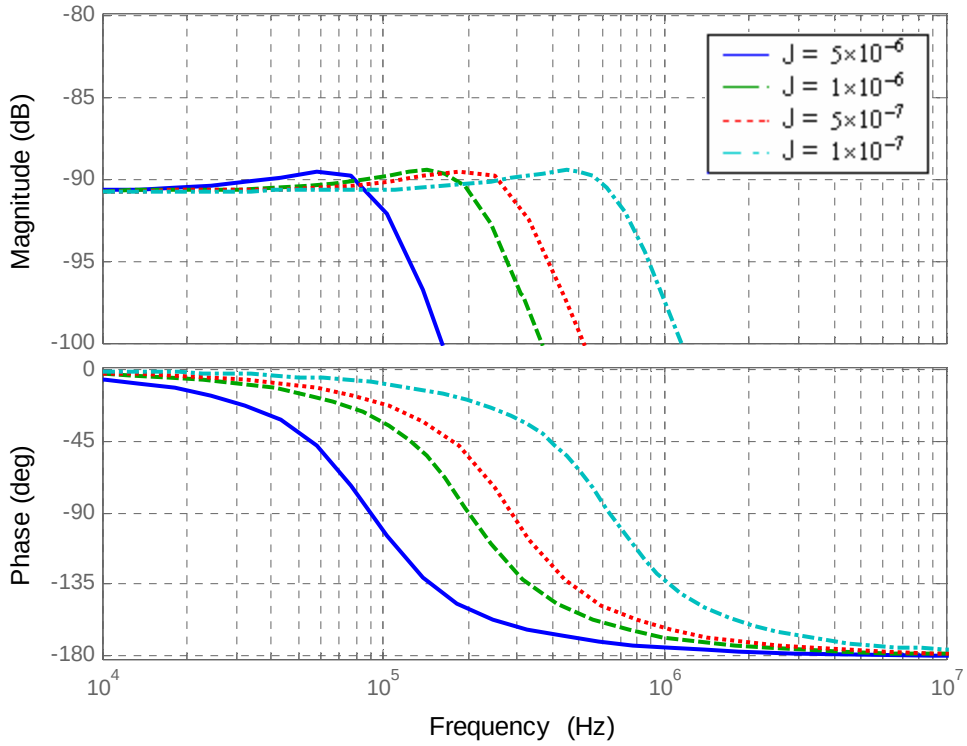

Figure 4.1.9: Frequency response of lateral actuator at a variety of J values (10 kHz-10 MHz).

In the proposed actuator system, the rotational mass moment of inertia $J = 3.6667 \times 10^{-7}\,\mathrm{kg \cdot mm^2}$. The value of the rotational moment of inertia is changed from $5 \times 10^{-6}\,\mathrm{kg \cdot mm^2}$ to $1 \times 10^{-7}\,\mathrm{kg \cdot mm^2}$. **Figure 4.1.8** and **Figure 4.1.9** show that if J is decreasing, the servo bandwidth and resonance frequency are increasing. Because the rotational moment of inertia is proportional to the size and mass of the slider, reducing the size and mass of the slider is required to achieve better performance. Since a

conventional Pico size slider is used in this study, the value of J does not change. However, with this knowledge, using smaller and lighter sliders, or using head driven actuator designs can be considered.

4.2 Frequency Response of the Transverse Actuator

In this section, the system frequency response of the transverse piezoelectric microactuator is given, followed by discussion of target performance evaluation. The frequency responses of the actuator system with various system parameters are presented. This study can be used for future design improvement.

4.2.1 Characteristics of the transverse actuator

As mentioned in Chapter Three, the dynamics of the actuator system in the first mode and at the end of the beam (x = L) is considered in this study. From Chapter Three, equation (3.2.41), (3.2.42-b) and (3.2.17), the dynamic equation of the piezoelectric transverse actuator in the first mode and at the end of the beam is defined by

$$\ddot{u}_3 + 2\zeta_1\omega_1\dot{u}_3 + \omega_1^2 u_3 = U_{31}(L)\,F_1^* \sin\omega t \tag{4.2.1}$$

where

$$F_1^* = \frac{Y\ d_{31}\ b\ h V_0}{L^2 \rho N_1}\int_o^L U_{31}dx \tag{4.2.2}$$

$$N_1 = \int_o^L (U_{31})^2 dx \tag{4.2.3}$$

The system equation (4.2.1) can be expressed in state-variable form with a control voltage input and a displacement output. Let $x_1 = u_3$, $x_2 = \dot{x}_1 = \dot{u}_3$, and the control input be u. The system equation (4.2.1) is expressed as a matrix form defined by

$$\begin{bmatrix} \dot{x}_1 \\ \dot{x}_2 \end{bmatrix} = \begin{bmatrix} 0 & 1 \\ -\omega_1^{\,2} & -2\zeta_1\omega_1 \end{bmatrix} \begin{bmatrix} x_1 \\ x_2 \end{bmatrix} + \begin{bmatrix} 0 \\ U_{31}(L)\, F_1^{*} \end{bmatrix} u \tag{4.2.4}$$

Let the output $y = x_1$ be the head position in the transverse direction. The system can be expressed by

$$\begin{aligned} \dot{\mathbf{x}} &= \mathbf{F}\mathbf{x} + \mathbf{G}u \\ y &= \mathbf{H}\mathbf{x} + Ju \end{aligned} \tag{4.2.5}$$

where,

$$\mathbf{F} = \begin{bmatrix} 0 & 1 \\ -\omega_1^{\,2} & -2\zeta_1\omega_1 \end{bmatrix} \tag{4.2.6}$$

$$\mathbf{G} = \begin{bmatrix} 0 \\ U_{31}(L)\, F_1^{*} \end{bmatrix} \tag{4.2.7}$$

$$\mathbf{H} = \begin{bmatrix} 1 & 0 \end{bmatrix} \tag{4.2.8}$$

$$J = 0 \tag{4.2.9}$$

The transfer function of the transverse actuator with a control voltage input and a displacement output is obtained by using MATLAB.

$$G_{PZT} = \frac{4.657 \times 10^{-10} s + 1.735 \times 10^{7}}{s^2 + 3.718 \times 10^{6} s + 1.382 \times 10^{13}} \tag{4.2.10}$$

Figure 4.2.1 and **Figure 4.2.2** show the frequency response of the transverse actuator. Bode plot is used for displaying of the frequency response of the system.

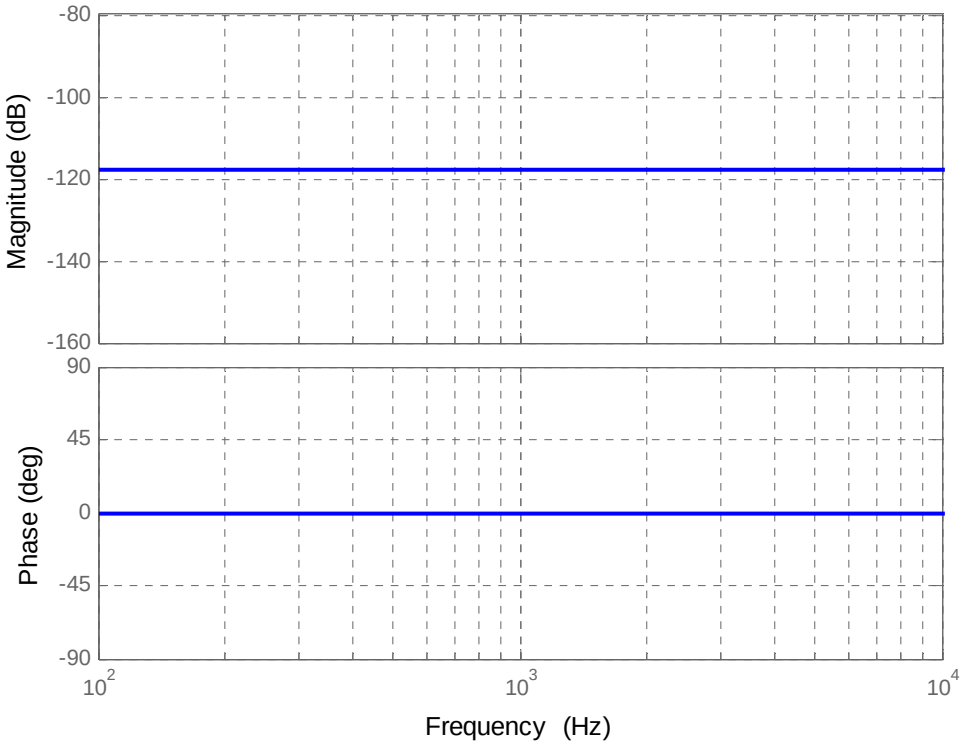

Figure 4.2.1: Frequency response of transverse actuator (100 Hz-10 kHz).

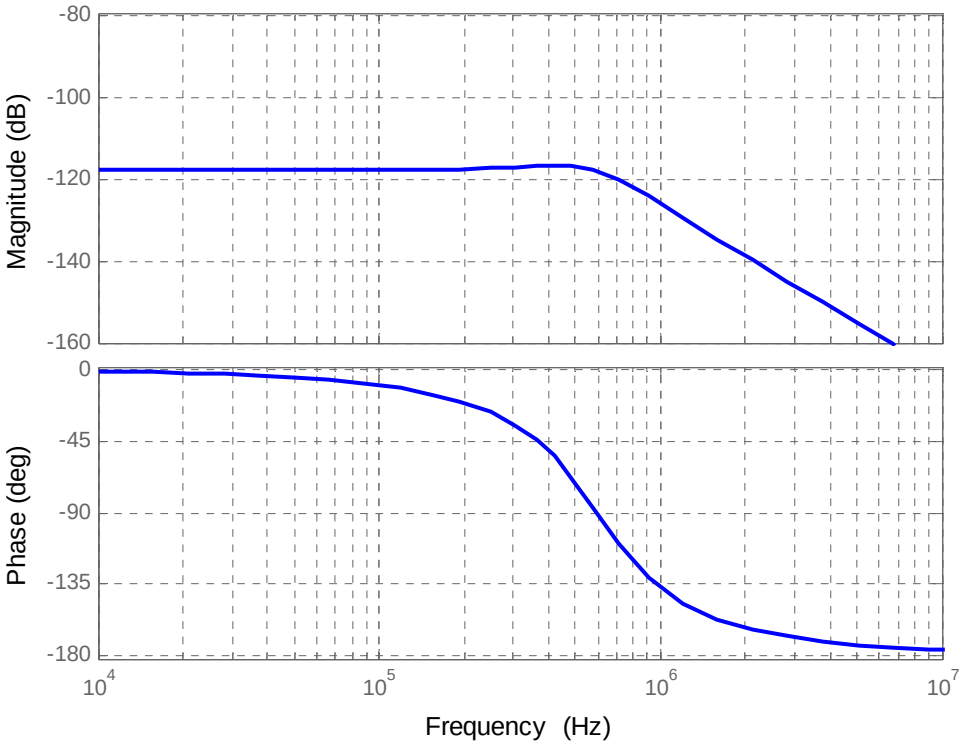

Figure 4.2.2: Frequency response of transverse actuator (10 kHz-10 MHz).

In Chapter Two, **Table 2.2.2,** the target resonance frequency was set to 100 kHz. The frequency response shows that the proposed piezoelectric actuator achieved resonance frequency of more than 100 kHz under the 0.5 % damping assumption which is satisfies the target requirements.

4.2.2 Frequency response of the transverse actuator with a variety of system parameters

Fast and precise flying-height adjustment allows improving read/write operations for high density hard disk drives. Understanding how system parameters affect the performance of

the actuator system is helpful to improve the design of actuators. For this purpose, the frequency responses of the system with a variety of system parameters are presented in this section.

Damping ratio

The effect of the damping ratio to the transverse actuator system is obtained. **Figure 4.2.3 and Figure 4.2.4** show the system frequency response with different values of damping ratio.

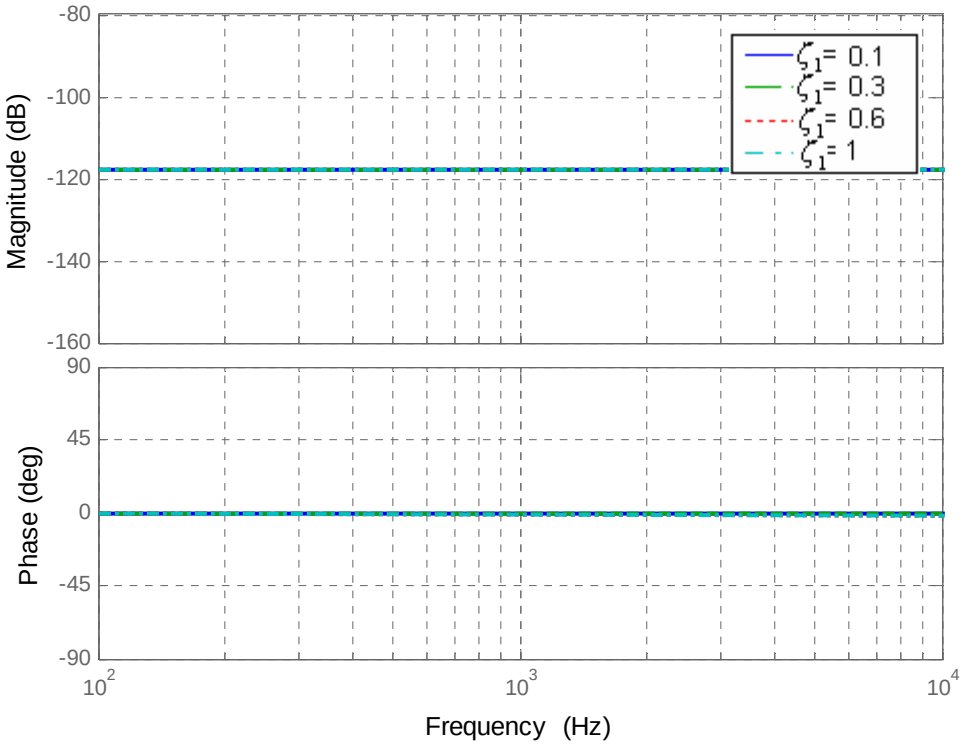

Figure 4.2.3: Frequency response of transverse actuator at a variety of ζ_1 values (100 Hz-10 kHz).

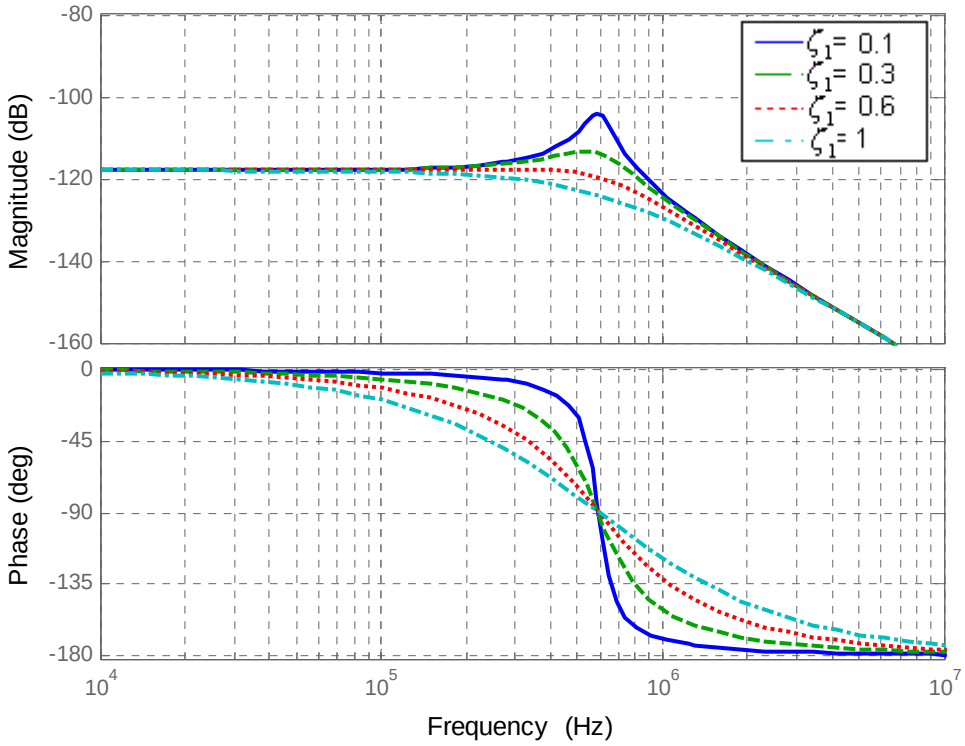

Figure 4.2.4: Frequency response of transverse actuator at a variety of ζ_1 values (10 kHz-10 MHz).

In the proposed system, the damping ratio in the first mode $\zeta_1 = 0.5$. The value of the damping ratio is changed from 0.1 to 1. **Figure 4.2.3** and **Figure 4.2.4** show that the damping ratio ζ_1 does not change the mechanical resonant frequency. However, damping has a large influence on the amplitude and phase angle in the frequency region near resonance. If the damping ratio is decreasing, the servo bandwidth is increasing. Decreasing the damping ratio is required to achieve high servo bandwidth.

Natural frequency

The effect of the natural frequency to the transverse actuator is obtained**. Figure 4.2.5** and **Figure 4.2.6** show the system frequency response with different values of the natural frequency.

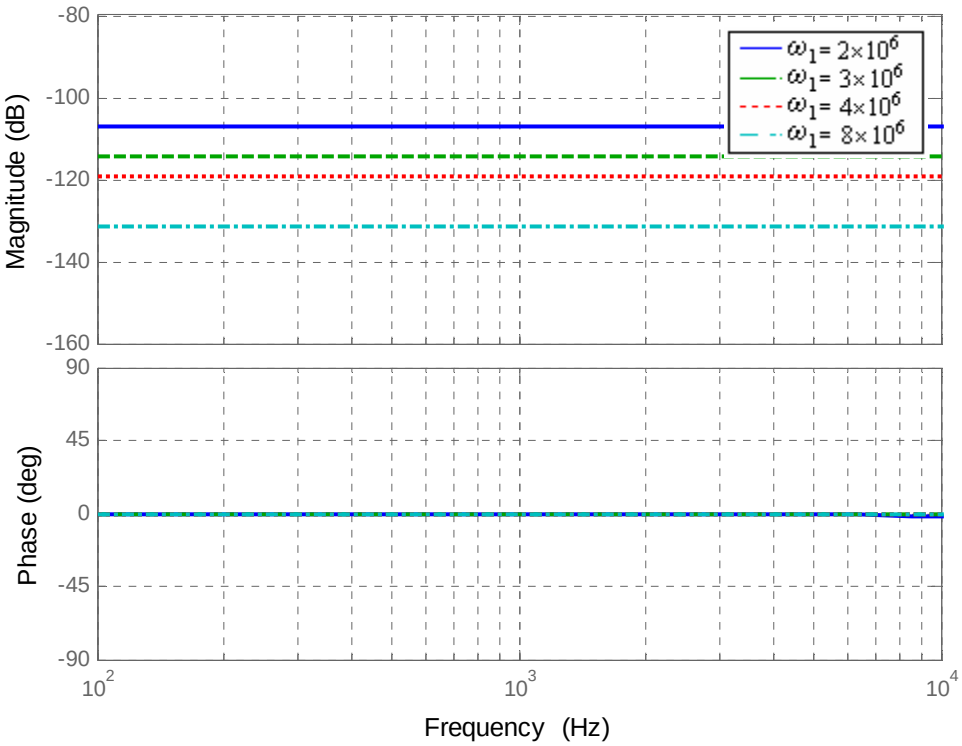

Figure 4.2.5: Frequency response of transverse actuator at a variety of ω_1 values (100 Hz-10 kHz).

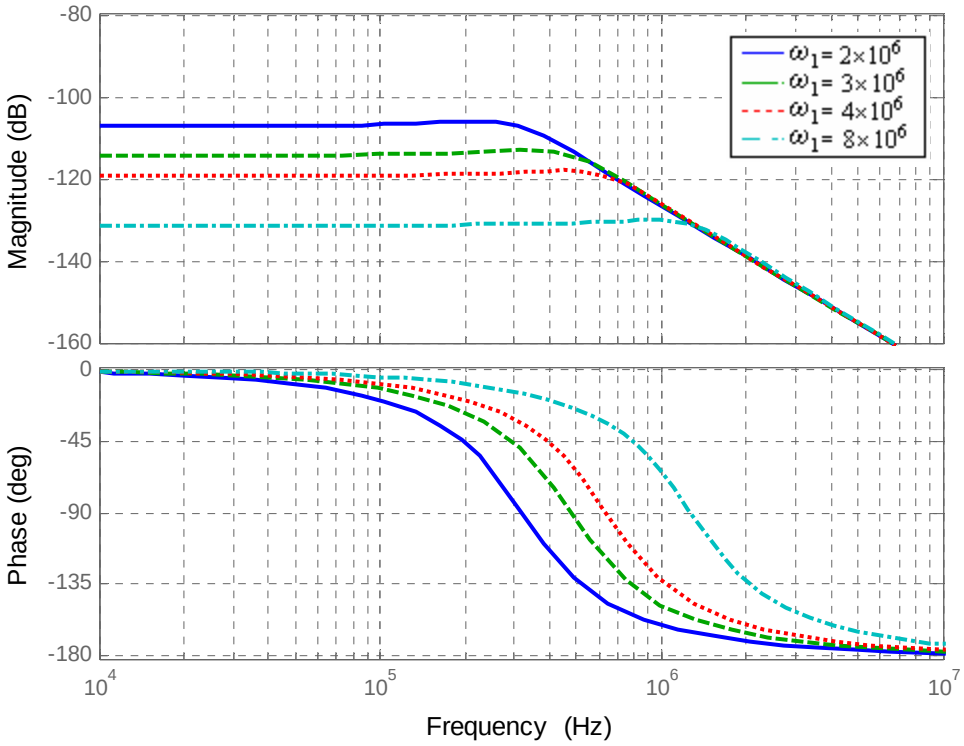

Figure 4.2.6: Frequency response of piezoelectric actuator at a variety of ω_1 values (10 kHz-10 MHz).

In the proposed actuator system, the natural frequency in the first mode $\omega_1 = 3.718\times10^6$. The value of the natural frequency of the system is changed from 2×10^6 to 8×10^6. **Figure 4.2.5** and **Figure 4.2.6** show that if ω_1 is increasing, the resonance frequency is also increasing. From Chapter Three, equation (3.2.43) and (3.2.26), ω_1 is defined by

$$\omega_1 = \sqrt{\frac{Y_p h^2}{12\rho_p}} \left(\frac{1.875}{L}\right)^2 \tag{4.2.11}$$

To increase ω_1, reducing the length of the actuator, increasing the thickness, or choosing the material with higher Young's modulus and lower density are needed. Since these variables are also related with the lateral and transverse displacement, size and shape of the actuator, changing these values should be considered carefully. The frequency response analysis shows that the proposed piezoelectric actuator satisfies the target requirements which were defined in Chapter Two under the 0.5 % damping assumption. For future design improvement, the frequency responses of the system with a variety of system parameters are evaluated. Higher natural frequency, lower damping ratio, and smaller mass are required for better performance.

Chapter Five
Controller Design for the Actuator System

In this chapter, controller designs for the voice coil motor (VCM) and the piezoelectric micro actuator are given. Control is the process of causing a system variable to conform to some desired values. In this hard disk positioning system, lateral and transverse displacement are the system variables being controlled. Feedback control is used for precise control. The overall control scheme is given first, followed by the controller design for each actuator, i.e., the VCM actuator, the lateral Lead Zirconate Titanate (PZT) microactuator and the transverse PZT microactuator.

5.1 Overall Flow

Figure 5.1.1 shows the overall flow chart of the system. First, the lateral piezoelectric microactuator is working to place the head at the desired position. After the head position in the lateral direction is confirmed, the transverse piezoelectric microactuator works to place the head at the desired height. If all conditions are satisfied, read/write processing is started. To compensate for noise, actuators in both directions are still working during the read/write process. Three controllers are used for the head control: a track seeking controller for the VCM actuator, a track following controller for the lateral actuator and a height adjusting controller for the transverse actuator.

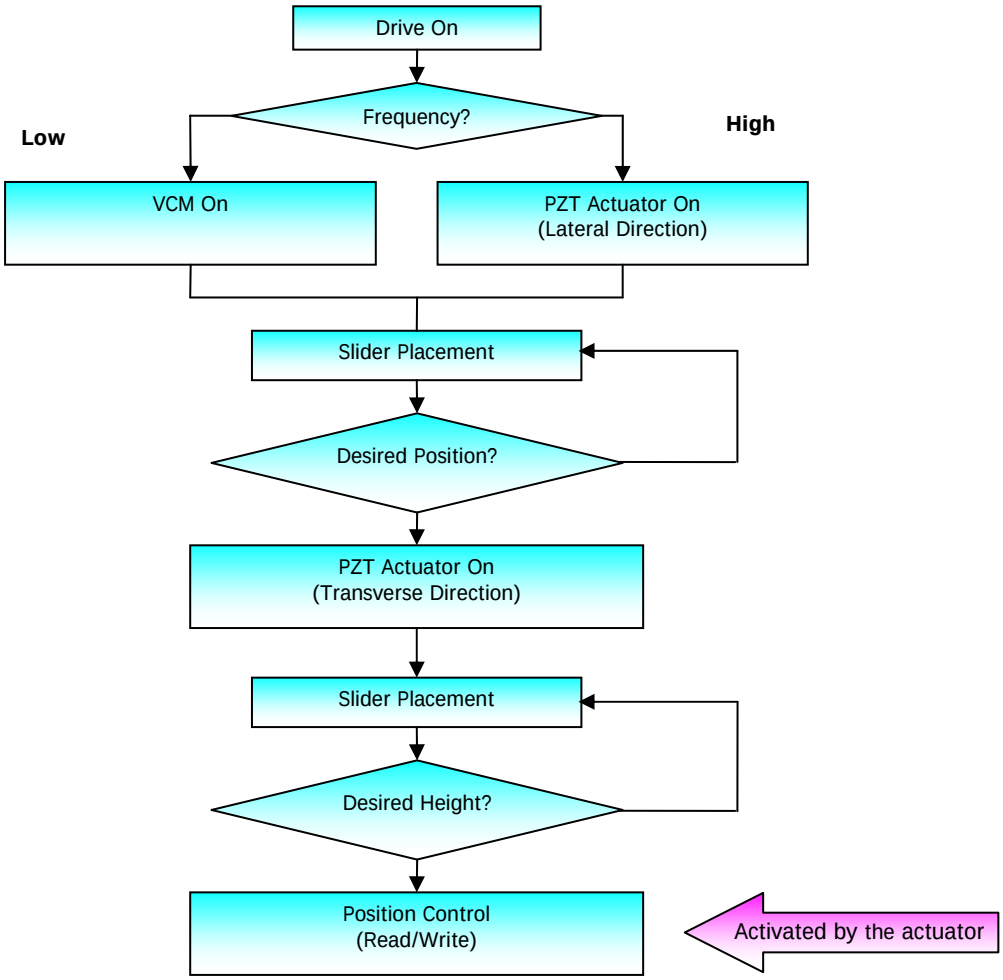

Figure 5.1.1: Overall flow chart of the actuator system.

5.2 Controller Design for Actuators in the Lateral Direction

In the VCM and microactuator dual stage servo system, the conventional VCM actuator is used as a primary actuator that controls the lower frequency part of the system and the microactuator is used as secondary actuator that controls the high frequency part. **Figure**

5.2.1 is shown the block diagram of dual actuator system.

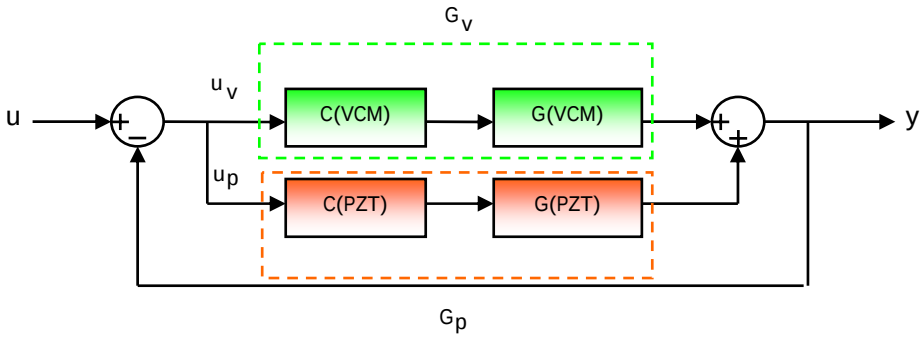

Figure 5.2.1: Block diagram of dual actuator system.

where C(VCM) is the transfer function of the controller for VCM; G(VCM) is the transfer function of VCM; C(PZT) is the transfer function of the controller for PZT actuator; G(PZT) is the transfer function of the PZT microactuator; G_P is the transfer function of the PZT actuator with controller and G_V is the transfer function of the VCM actuator with controller. From the **Figure 5.2.1**, displacement output is defined by

$$y = u_P G_P + u_V G_V \tag{5.2.1}$$

Controller design for the lateral control can be divided into two parts, i.e., the track seeking and track following parts. A track seeking controller is used to regulate the VCM and a track following controller is used to regulate the PZT actuator. Therefore, equation

(5.2.1) can be expressed by

$$y \approx u_P G_P \tag{5.2.2}$$

at high frequencies and expressed by

$$y \approx u_V G_V \tag{5.2.3}$$

at low frequencies where the cut-off frequency is target at 1kHz based on results of frequency response of the actuator system from Chapter Four.

5.2.1 Track seeking control for VCM

Track seeking control for a hard disk drive (HDD) ensures that an actuator moves to a target track address within a specified time. Since there are a lot of VCM actuator controller designs available, one of the controllers designed by Venkataramanan et al. (2002) [16] for the VCM control is selected. Maxtor HDD (Model 51536U3) is used for simulation in his study. The transfer function of the system is as follows: [16]

$$G(VCM) = \frac{6.4013 \times 10^7}{s^2} \times \frac{2.467 \times 10^8}{(s^2 + 2.513 \times 10^3 s + 2.467 \times 10^8)} \tag{5.2.4}$$

A proximate time-optimal servomechanism (PTOS) controller for track seeking is used in his study. **Figure 5.2.2** shows the block diagram of track seeking control.

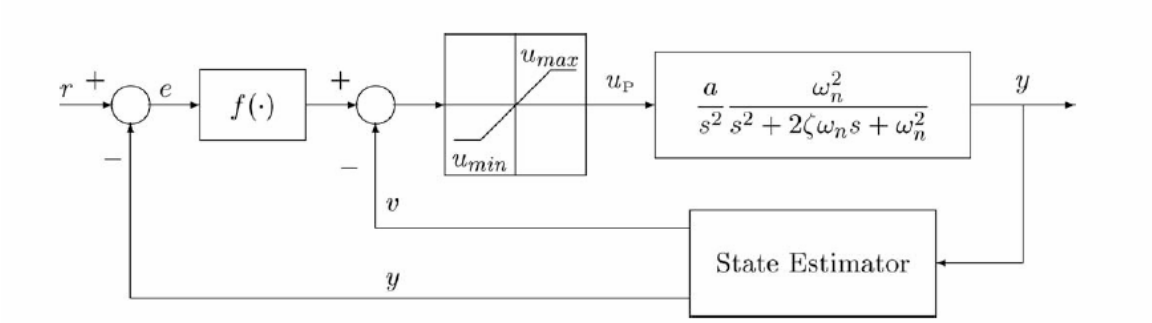

Figure 5.2.2: Block diagram of track seeking control system (Venkataramanan et al., 2002) [16].

Figure 5.2.3 and **Figure 5.2.4** show simulation results of the system response. In his study, MATLAB is used for simulation.

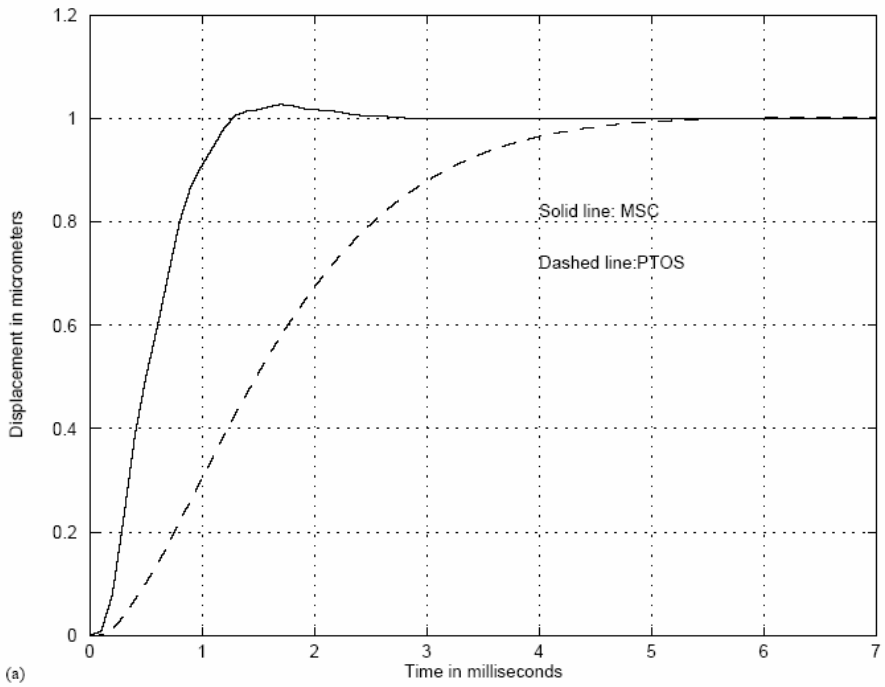

Figure 5.2.3: Response for 1 μm displacement (Venkataramanan et al., 2002) [16].

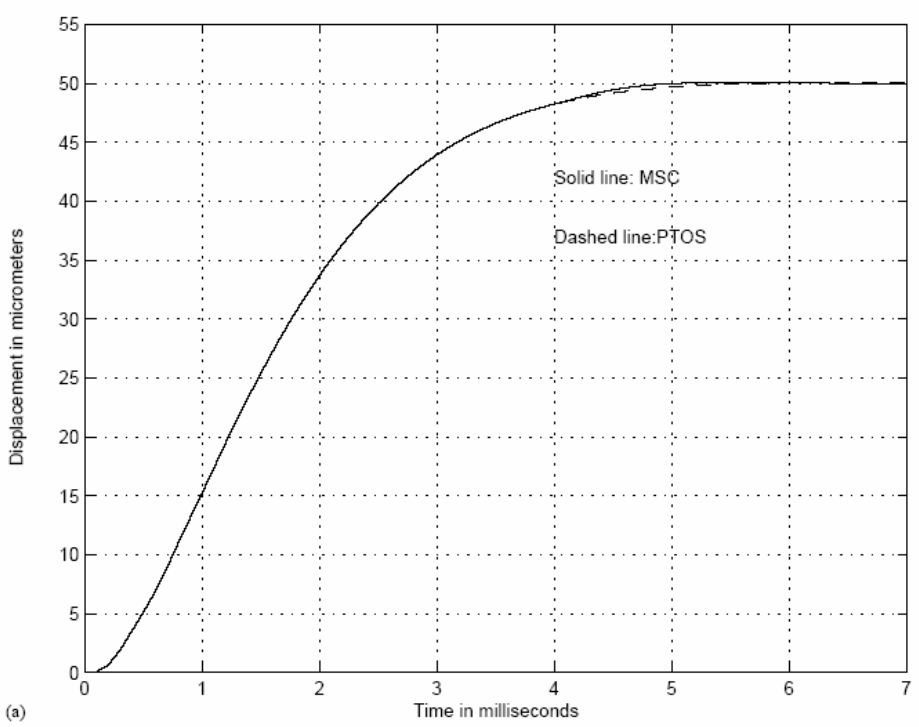

Figure 5.2.4: Response for 50 μm displacement (Venkataramanan et al., 2002) [16].

.

5.2.2 Track following control for the lateral actuator

The purpose is to find compensation D (PZT) to achieve better track following control, such as that shown in **Figure 5.2.5**.

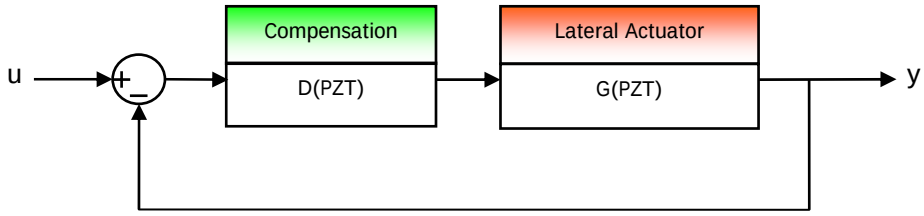

Figure 5.2.5: Block diagram of the lateral actuator system.

In this section, the state-space design method is used to design a controller. The state-space design method has several steps. First, we need to select pole locations which satisfy the requirements and develop the control law and estimator for the closed-loop system that corresponds to satisfactory dynamic response and then combine the control law and the estimator.

Selection of pole locations for control law

The dominant second-order poles method is used for pole placement. From the Chapter Four, equation (4.1.11), the transfer function of the lateral actuator system is defined as

$$G_{pzt} = \frac{-6.985\times10^{-10}s + 1.273\times10^{8}}{s^{2} + 2.094\times10^{6}s + 4.385\times10^{12}} \tag{5.2.5}$$

The pole locations of the system are obtained by using MATLAB.

$$\text{Pole} = \left[-1.047\times10^{6} + 1.814\times10^{6}i \quad -1.047\times10^{6} - 1.814\times10^{6}i\right] \tag{5.2.6}$$

The pole locations of the system in s-plane are shown in **Figure 5.2.6.**

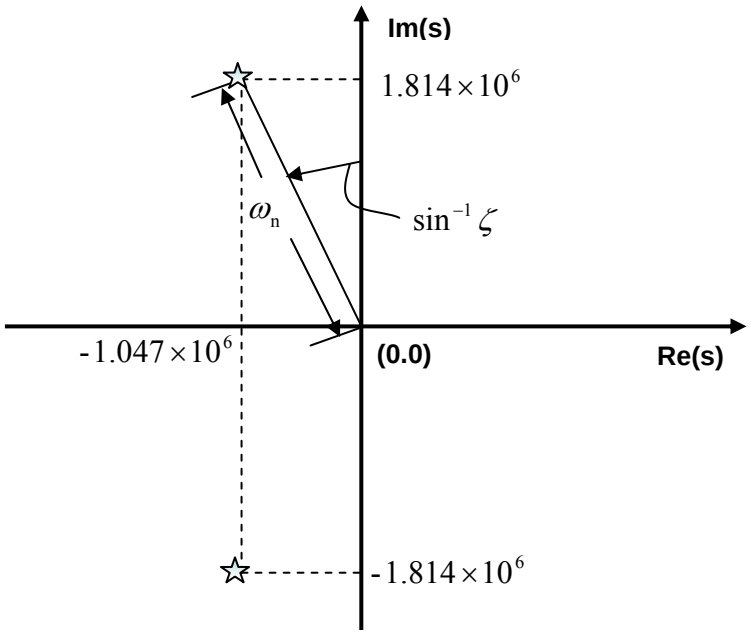

Figure 5.2.6: Pole locations of the lateral microactuator.

The poles of this transfer function are located at a radius ω_n in the s-plane and at an angle $\sin^{-1}\zeta$. The shapes of the time response of the system are determined by the poles of the system. **Figure 5.2.7** shows the relationship between pole locations and time response.

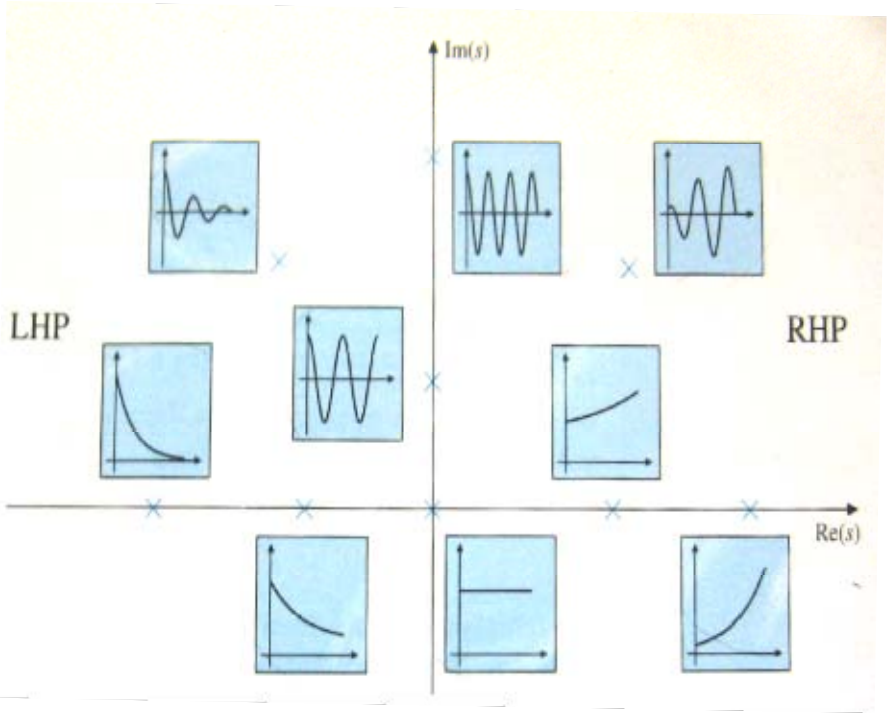

Figure 5.2.7: Time functions associated with pole position (Franklin et al., 1995) [19].

In general, poles father to the left in the s-plane decay faster than poles closer to the imaginary axis. **Figure 5.2.8** shows the time response of the lateral actuator for $0.1\ \mu$m displacement.

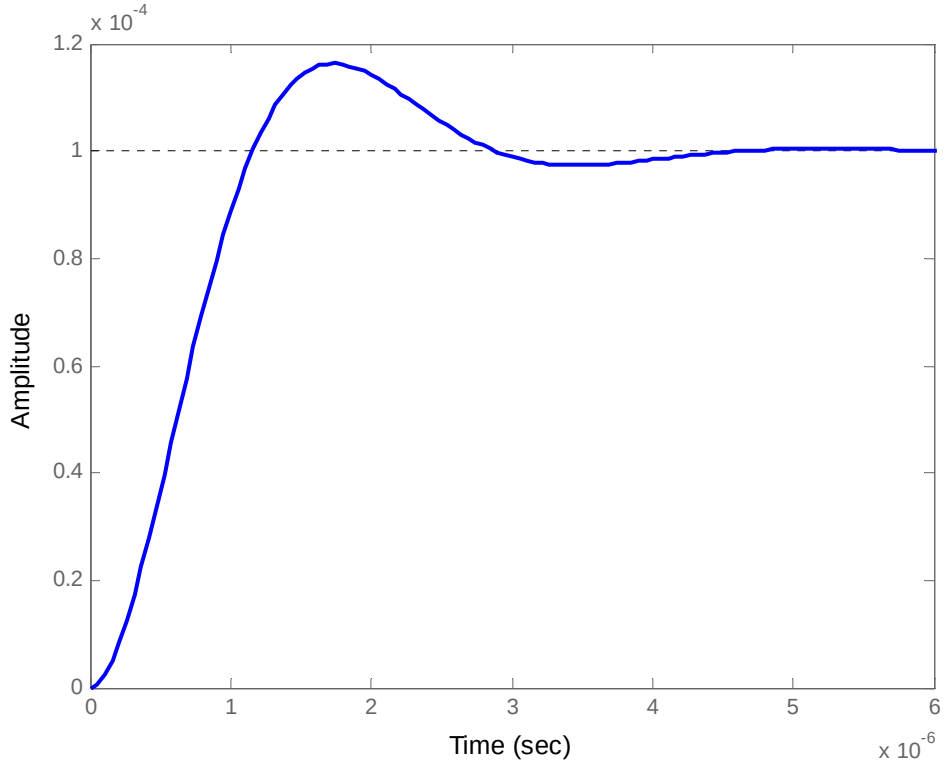

Figure 5.2.8: Time response of the lateral microactuator (response for $0.1\,\mu$m displacement).

The rise time, the settling time and the overshoot of the system are important factors to show characteristics of the time response. The rise time is a measure of how long the system takes to be translated from one position to another (10-90%). The overshoot is the percentage of the highest overshoot of the system. The settling time is the time required to reach and stay within a tolerance band of the final value (1%). By using a controller, the rise time, the settling time and the overshoot of the system can be decreased for better

time response. The rise time of the system is typically related to pole location parameter ω_n, the overshoot of the system is typically related to pole location parameter ζ and the settling time is typically related to pole location parameters ω_n and ζ. For a second-order system with no finite zeros, the transient response parameters can be approximated in the following way. The rise time of the system is defined by

$$t_r \cong \frac{1.8}{\omega_n} = \frac{1.8}{2.094 \times 10^6} = 8.596 \times 10^{-7} \tag{5.2.7}$$

The overshoot of the system is defined by

$$M_p = e^{-\frac{\pi\zeta}{\sqrt{1-\zeta^2}}} = e^{-\frac{\pi\, 0.5}{\sqrt{1-0.5^2}}} = 0.163 \tag{5.2.8}$$

The settling time of the system is defined by

$$t_s = \frac{4.6}{\zeta\, \omega_n} = \frac{4.6}{0.5 \cdot 2.094 \times 10^6} = 4.394 \times 10^{-6} \tag{5.2.9}$$

The time takes for track seeking is called "seek time". A typical seek time for a hard disk is about 9 ms. Comparing to a typical seek time, the settling time of the microactuator system is insignificant. However, the actuator system has relatively high overshoot. To compensate for this overshoot, the pole locations which limit overshoot to no more than 5 % are chosen. From the plots of the second-order transients in **Figure 5.2.9**, a damping ratio $\zeta = 0.7$ will meet the overshoot requirement.

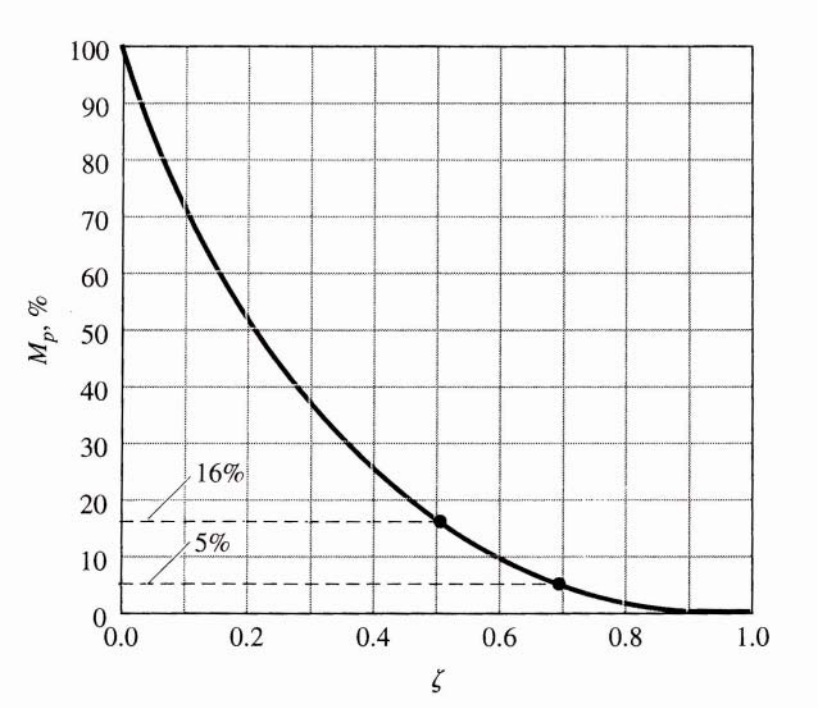

Figure 5.2.9: Overshoot versus damping ratio for the second-order system (Franklin et al., 1995) [19].

Pole locations corresponding to $\zeta = 0.707$ are shown in **Figure 5.2.10**.

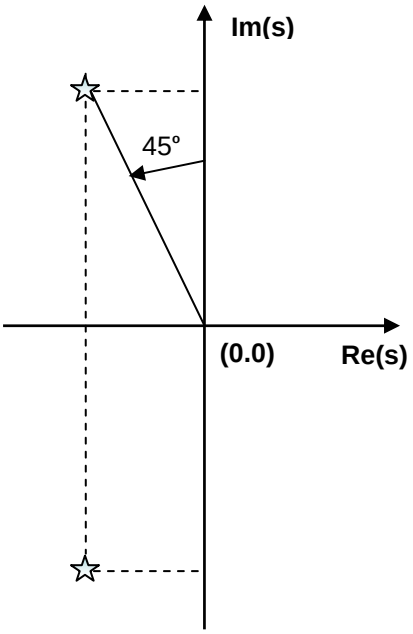

Figure 5.2.10: Pole locations corresponding to $\zeta = 0.707$.

From all considerations above, the desired poles are selected as

$$\text{Pole} = \left[-1.481\times10^{5} + 1.481\times10^{5}\,\text{i} \quad -1.481\times10^{5} - 1.481\times10^{5}\,\text{i}\right] \tag{5.2.10}$$

The desired pole locations in s-plane are shown in **Figure 5.2.11.**

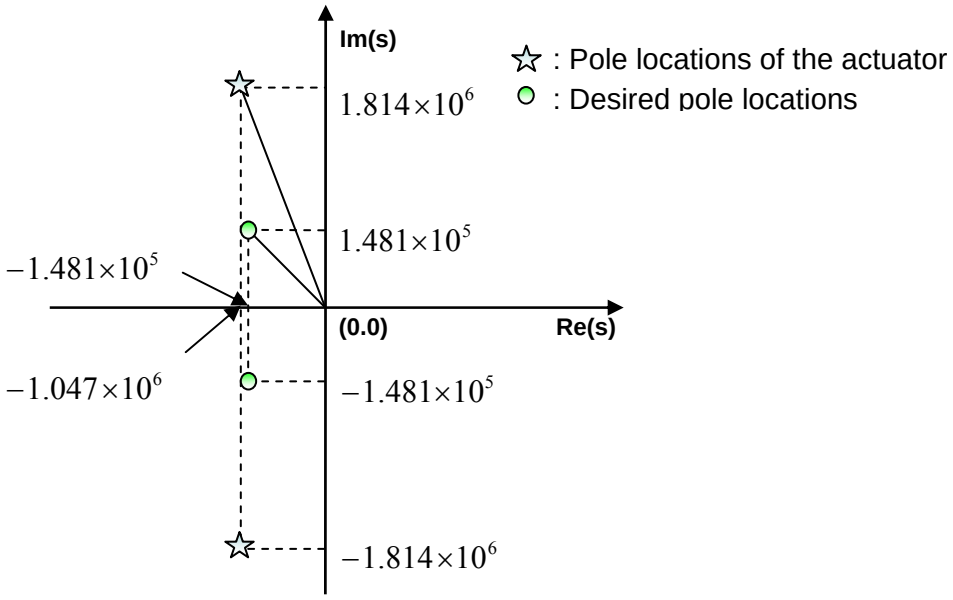

Figure 5.2.11: Desired pole locations for the lateral microactuator.

Although selected pole locations have disadvantages to the rise time of $8.6\mu s$ and settling time of $27\mu s$, these disadvantages are insignificant comparing with a typical seek time of 9ms.

Control law design

The purpose of the control law is to allow us to assign a set of pole locations for the closed-loop system that will correspond to satisfactory dynamic response in terms of the rise time, the settling time and the overshoot of transient response. We need to find the control law K as feedback of a linear combination of the state variables as shown in equation (5.2.11).

$$u = -\mathbf{K}\mathbf{x} = -\begin{bmatrix} K_1 & K_2 & \cdots & K_n \end{bmatrix} \begin{bmatrix} x_1 \\ x_2 \\ \vdots \\ x_n \end{bmatrix} \tag{5.2.11}$$

The system has a constant matrix in the state-vector feedback path as shown in **Figure 5.2.12**.

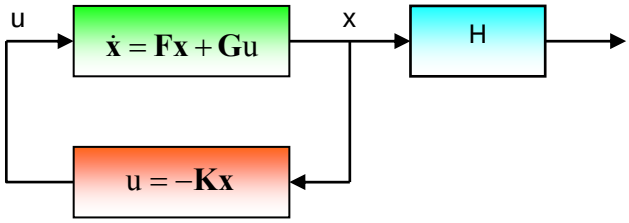

Figure 5.2.12: Assumed system for control-law design (Franklin et al., 1995) [19].

Substituting the feedback law $u = -\mathbf{K}\mathbf{x}$ in to the system equation $\dot{\mathbf{x}} = \mathbf{F}\mathbf{x} + \mathbf{G}u$ yields

$$\dot{\mathbf{x}} = \mathbf{F}\mathbf{x} - \mathbf{G}\mathbf{K}\mathbf{x} \tag{5.2.12}$$

The characteristic equation for this close-loop system is

$$\det[\, s\mathbf{I} - (\mathbf{F} - \mathbf{G}\mathbf{K})] = 0 \tag{5.2.13}$$

The control law consists of picking the gain **K** so that the roots of equation (5.2.13) are in desirable locations. If desired pole locations are known, MATLAB function "acker" can be used to determine the control law. MATLAB function "acker" gives the control law for the previously chosen pole locations.

$$K = \left[-3.411 \times 10^{4} \quad -0.014 \right] \tag{5.2.14}$$

Estimator design

In the control law design, all the state variables are available for feedback was assumed. In most case, not all the state variables are measured. We need the estimate of the state and to reconstruct the state variables. Let $\hat{x}$ be the estimate of the system. We need to consider feeding back the difference between the measured and estimated outputs and correcting the model continuously with this error as shown in **Figure 5.2.13**.

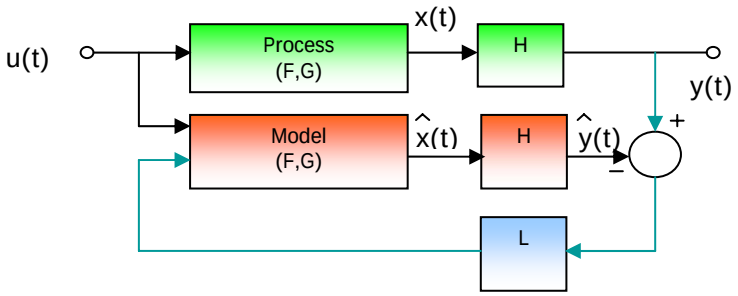

Figure 5.2.13: Closed-loop estimator (Franklin et all, 1995) [19].

The estimator should be chosen to achieve satisfactory error characteristic. If desired pole locations are known, MATLAB function "acker" can be used to determine the estimator. The estimator poles can be chosen to be faster then the controller poles. This ensures a faster decay of the estimator errors compared with the desired dynamics, thus causing the controller poles to dominate the total response. Equation (5.2.15) shows the chosen pole locations.

$$\text{Pole} = \left[-1.047\times10^{6} + 1.814\times10^{6}\,\text{i} \quad -1.047\times10^{6} - 1.814\times10^{6}\,\text{i}\right] \tag{5.2.15}$$

MATLAB function "acker" gives the estimator for chosen pole locations.

$$\text{L} = \begin{bmatrix} 0.209 \\ 4.385\times10^{5} \end{bmatrix} \tag{5.2.16}$$

Combine the control law and the estimator

If the control law and the estimator described above are combined, the design is complete for a compensator that is able to reject disturbances. The compensator transfer function is given by

$$\text{D(s)} = \frac{\text{U(s)}}{\text{Y(s)}} = -\mathbf{K}(\text{s}\mathbf{I} - \mathbf{F} + \mathbf{GK} + \mathbf{LH})^{-1}\mathbf{L} \tag{5.2.17}$$

Therefore, the transfer function of the compensator is defined by

$$\text{D(s)} = \frac{1.334\times10^{4}\,\text{s} + 1.694\times10^{10}}{\text{s}^{2} + 2.962\times10^{5}\,\text{s} + 4.386\times10^{10}} \tag{5.2.18}$$

Now, the transfer functions of both the compensation and piezoelectric microactuator are obtained.

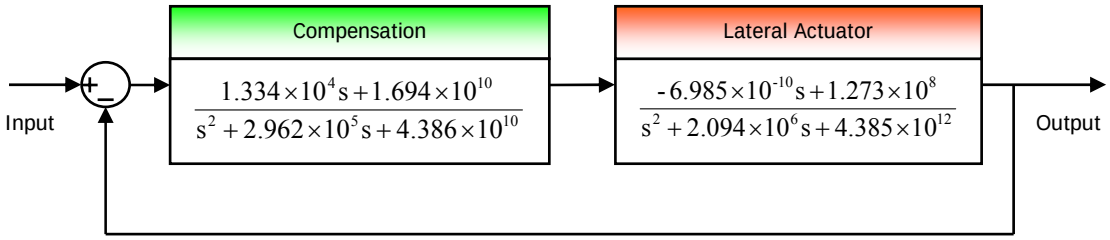

Figure 5.2.14: Block diagram of track following control system.

The time response of the closed-loop system for $0.1\,\mu$m displacement is shown **Figure 5.2.15**.

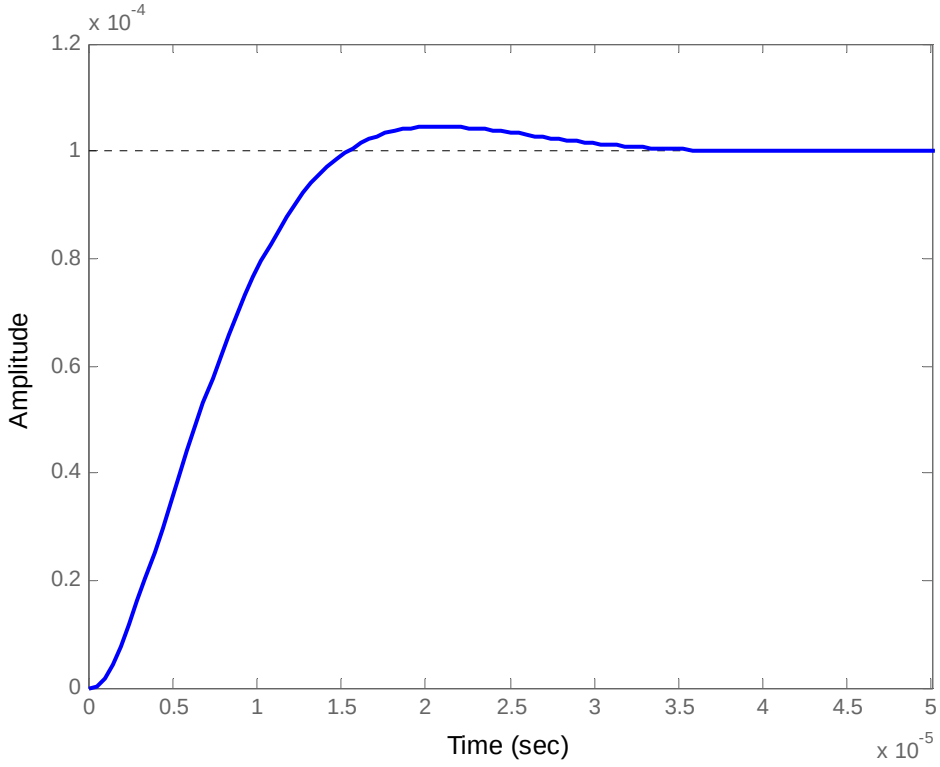

Figure 5.2.15: Time response of the lateral microactuator with the compensator (response for $0.1\,\mu$m displacement).

The time response of the lateral microactuator with the compensator shows that the overshoot of the lateral actuator system are reduced.

5.3 Controller Design for the Transverse Actuator

For the transverse actuator, the flying height is the system variable being controlled. The purpose is to find a compensation D(PZT) to achieve better flying height control, such as that shown in **Figure 5.3.1**. First, we need to select pole locations which satisfy the requirements and develop the control law and estimator for the closed-loop system that corresponds to satisfactory dynamic response and then combine the control law and the estimator.

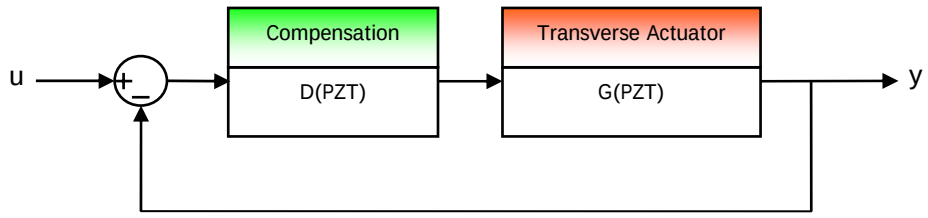

Figure 5.3.1: Block diagram of the transverse actuator system.

Control law design

The dominant second-order poles method is used for pole placement. From the Chapter Four, equation (4.2.10), the transfer function of the transverse actuator system is defined as

$$G_{PZT} = \frac{4.657\times10^{-10}s + 1.735\times10^{7}}{s^{2} + 3.718\times10^{6}s + 1.382\times10^{13}} \tag{5.3.1}$$

The pole locations of the system are obtained by using MATLAB.

$$\text{Pole} = \left[-1.859\times10^{6} + 3.220\times10^{6}i \quad -1.859\times10^{6} - 3.220\times10^{6}i\right] \tag{5.3.2}$$

The pole location of the system in s-plane is shown in **Figure 5.3.2**.

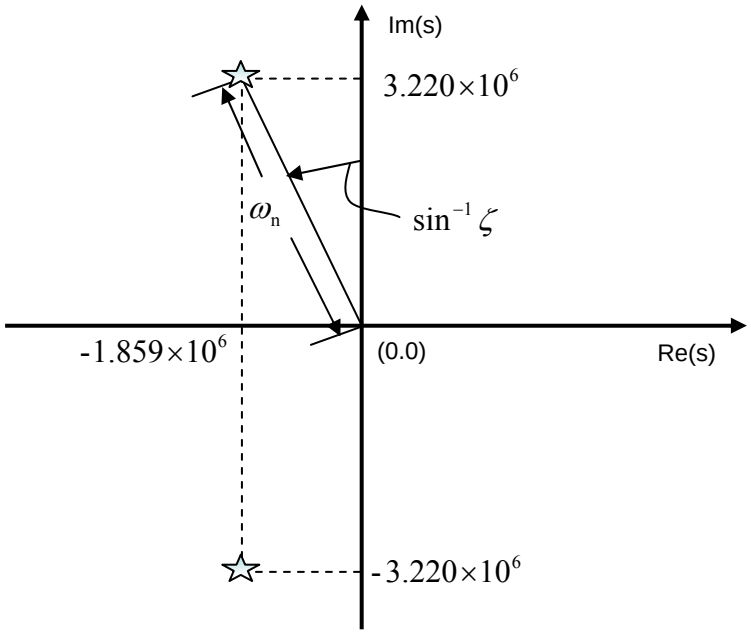

Figure 5.3.2: Pole locations of the transverse microactuator.

Figure 5.3.3 shows the time response of the transverse actuator for 19nm displacement.

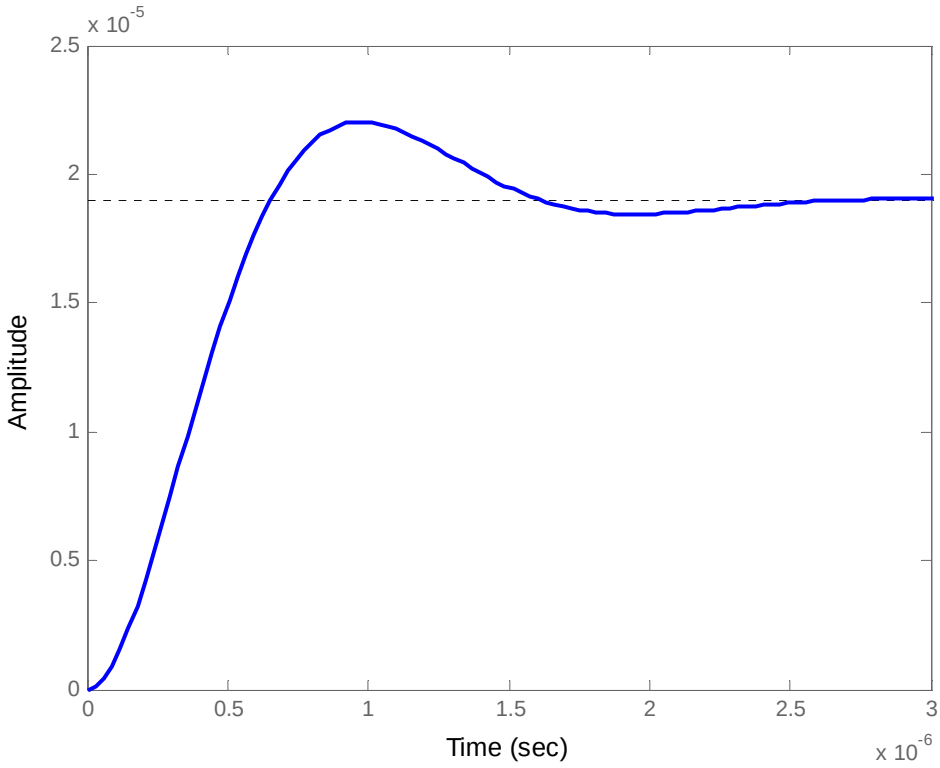

Figure 5.3.3: Time response of the transverse microactuator (response for 19nm displacement).

By using a controller, we can decrease the rise time, the settling time and the overshoot of the actuator system for better time response. The rise time of the system is defined by

$$t_r \cong \frac{1.8}{\omega_n} = \frac{1.8}{3.718 \times 10^6} = 4.841 \times 10^{-7} \tag{5.3.3}$$

The overshoot of the system is defined by

$$\mathrm{M_p} = \mathrm{e}^{-\frac{\pi\zeta}{\sqrt{1-\zeta^2}}} = \mathrm{e}^{-\frac{\pi\, 0.5}{\sqrt{1-0.5^2}}} = 0.163 \tag{5.3.4}$$

The settling time of the system is defined by

$$\mathrm{t_s} = \frac{4.6}{\zeta\ \omega_\mathrm{n}} = \frac{4.6}{0.5 \cdot 3.718 \times 10^6} = 2.474 \times 10^{-6} \tag{5.3.5}$$

A typical seek time for a hard disk is about 9 ms. Comparing with a typical seek time, the settling time of the microactuator system is insignificant. However, the actuator system has relatively high overshoot. To compensate for this overshoot, the pole locations which limit overshoot to no more than 5 % are chosen. From the plots of the second-order transients in **Figure 5.2.9**, a damping ratio $\zeta = 0.7$ will meet the overshoot requirement. From all considerations above, the desired poles are given by

$$\text{Pole} = \left[-2.629 \times 10^5 + 2.629 \times 10^5\,\mathrm{i} \quad -2.629 \times 10^5 - 2.629 \times 10^5\,\mathrm{i}\right] \tag{5.3.6}$$

The desired pole locations in s-plane are shown in **Figure 5.3.4.**

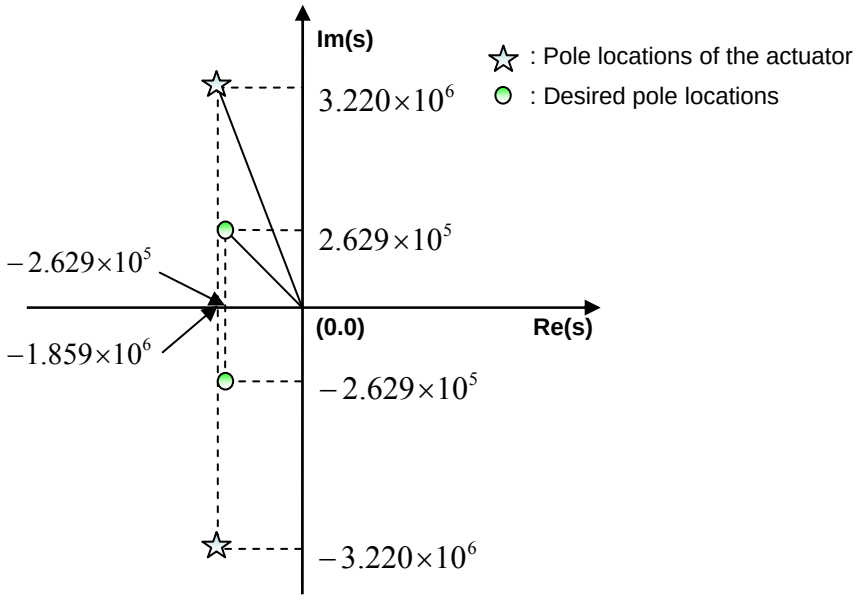

Figure 5.3.4: Desired poles locations for the transverse microactuator.

Although selected pole locations have disadvantages to the rise time of $4.36\mu s$ and settling time of $15\mu s$, these disadvantages are insignificant comparing with a typical seek time of 9ms. MATLAB function "acker" gives the control law for the previously chosen pole locations.

$$K = \begin{bmatrix} -7.887\times10^{5} & -0.184 \end{bmatrix} \tag{5.3.7}$$

Estimator design

The estimator should be chosen to achieve satisfactory error characteristic. The estimator poles can be chosen to be faster then the controller poles. This ensures a faster decay of

the estimator errors compared with the desired dynamics, thus causing the controller poles to dominate the total response. Equation (5.3.8) shows the chosen pole locations.

$$\text{Pole} = \left[-1.859\times10^{6} + 3.220\times10^{6}\,\text{i} \quad -1.859\times10^{6} - 3.220\times10^{6}\,\text{i}\right] \tag{5.3.8}$$

MATLAB function “acker” gives the estimator for chosen pole locations.

$$\text{L} = \begin{bmatrix} 0.372 \\ 1.382\times10^{6} \end{bmatrix} \tag{5.3.9}$$

Combine the control law and the estimator

If the control law and the estimator described above are combined, the design is complete for a compensator that is able to reject disturbances. The compensator transfer function is given by

$$\text{D(s)} = \frac{5.475\times10^{5}\,\text{s} + 1.235\times10^{12}}{\text{s}^{2} + 5.258\times10^{5}\,\text{s} + 1.382\times10^{11}} \tag{5.3.10}$$

Now, the transfer functions of both the compensation and piezoelectric transverse microactuator are obtained.

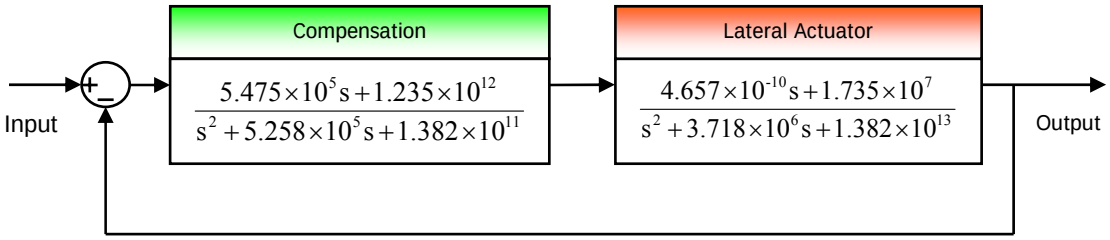

Figure 5.3.5: Block diagram of flying height adjusting control system.

The time response of the closed-loop system for 19nm displacement is shown **Figure 5.3.6.**

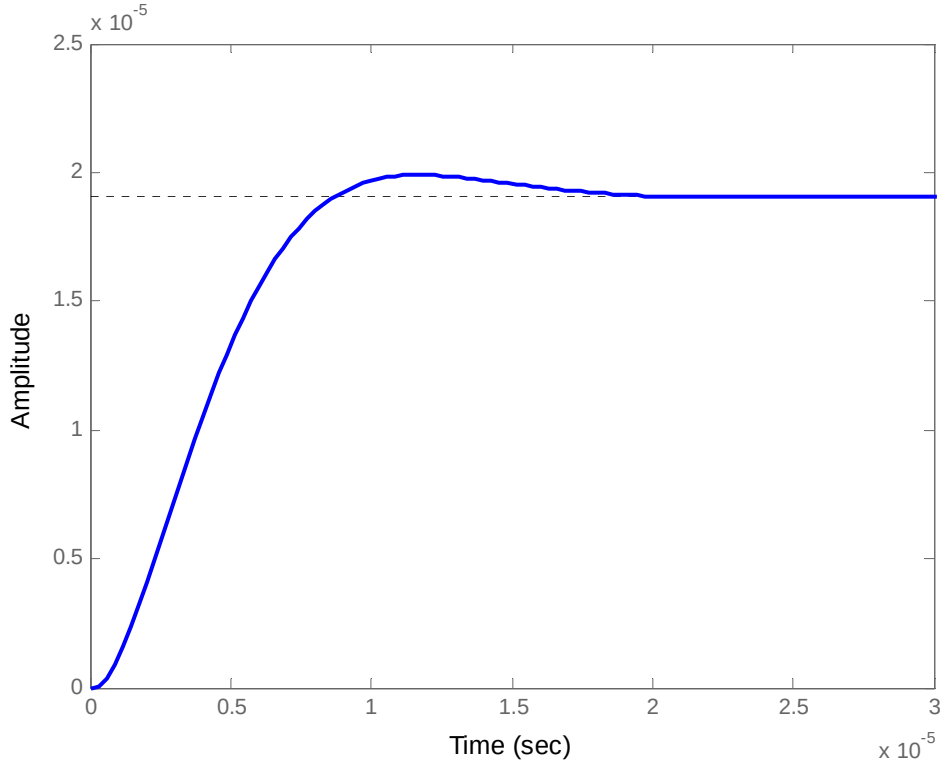

Figure 5.3.6: Time response of the transverse microactuator with the compensator (response for 19nm displacement).

The time response of the transverse microactuator with the compensator shows that the overshoot of the transverse actuator system are reduces. In this hard disk positioning system, the lateral and the transverse displacements were the system variables being controlled. The lateral actuator is working to place the head at the desired position and the transverse actuator works to place the head at the desired height. The state-space design method was used to design a controller. The proposed actuator systems have good rise time and settling time but relatively high overshoot. To compensate for these

overshoot, the pole locations which limit overshoot to no more than 5 % were chosen. Simulation results show that the overshoot and the fluctuation of the actuator system are reduced and response of the actuator system becomes more stable.

Chapter Six
Summary and Conclusions

The current trend in hard disk design is towards smaller hard disks with larger capacities. Areal density has been dramatically increasing at a rate of 100% a year. Hard disk drives of more than $30\,Gb/in^2$ areal densities are now available and research in the hard disk drives industry is now targeting an areal density of more than $100\,Gb/in^2$ or $1\,Tb/in^2$. Achieving such high storage density is possible by adjusting the movement of the head individually by using a microactuator integrated in the head positioning system. The use of piezoelectric microactuators for active control of the head positioning system in high density hard disk drives has recently become more common. The advantages of piezoelectric materials are their lightness, stiffness, large force generation, large displacement generation and temperature stability. For these reasons, Lead Zirconate Titanate 5 (PZT5) was chosen for use as the microactuator. The actuator uses the uniaxial actuation of PZT elements for the lateral control and the bimorph actuation of PZT elements for the transverse control. The purpose of this study was to 1) design a new piezoelectric microactuator with transverse and lateral control of head positioning systems for high density hard disk drives and 2) evaluate their performance.

6.1 Summary

The main objective of this research was to develop a new piezoelectric microactuator with transverse and lateral control of head positioning systems for high density hard disk drives and to evaluate their performance. Current research on microactuator design for high density hard disk drives was reviewed. The dual actuator system was proposed for fast and accurate head positioning in the lateral direction. The dual actuator design was divided into three types: a suspension driven actuator, a slider driven actuator and a head driven actuator. A self-adjusting flying height control slider was proposed for efficient head positioning in the transverse direction. In this study, a slider driven actuator with a self-adjusting flying height control was developed. Based on the current technology of

hard disk drive industries, $100\,\mathrm{Gb/in^2}$ areal density was set as a target density. For the $100\,\mathrm{Gb/in^2}$ areal density, the stroke of lateral displacement was set to be more than $0.2\,\mu\mathrm{m}$ $(\pm 0.1\,\mu\mathrm{m})$ with 5-6 kHz of servo bandwidth and the transverse deflection was set to be more than 19nm, corresponding to the flying height of less than 6 nm. The proposed microactuator had two actuation parts: the lateral actuator and the transverse actuator which were independently controlled. The lateral actuator worked to place the head at the desired position. After the head position in the lateral direction was confirmed, the transverse actuator worked to place the head at the desired height. If all conditions were satisfied, the read/write processing was started. The uniaxial deformation of piezoelectric materials was used to generate the lateral displacement and the bimorph deformation of piezoelectric materials was used to generate the transverse deflection. The dynamic equations of the piezoelectric microactuator were derived. Frequency response analyses of the actuator systems were conducted. A 0.5 % damping was assumed for evaluating the system performance in this study. Frequency response analysis using the state space method and Bode diagram showed that the proposed microactuator satisfied target requirements. The new actuator achieved maximum stroke of displacement of more than $0.2\,\mu\mathrm{m}$ with servo bandwidth of more than 6 kHz for the lateral motion and the flying height was decreased to less than 6 nm with resonance frequency of more than 100 kHz for the transverse motion under the 0.5 % damping assumption. Frequency responses with a variety of system parameters were evaluated for future improvement. For lateral control, higher natural frequency, lower damping ratio, or lower mass moment inertia were required for better performance. For transverse control, higher natural frequency or lower damping ratio were expected for better performance. Time response analyses of the actuator systems were conducted. The controllers in the closed-loop systems were designed to compensate for disturbances. In this hard disk positioning system, displacements in the lateral and the transverse directions were the system variables being controlled. Three controllers were used: a track seeking controller for the VCM actuator, a track following controller for the lateral PZT actuator, and a height adjusting controller for the transverse PZT actuator. Simulation results demonstrated the effectiveness of the proposed controller.

6.2 Conclusions

The purpose of the study is to develop a new piezoelectric microactuator with lateral and transverse control of head positioning systems in order to improve performance of high density hard disk drives by increasing servo bandwidth and decreasing flying height. In order to achieve two-dimensional controls, the microactuator, which has two actuation parts for the lateral and the transverse directions in a single body, is proposed. The axial deformation of piezoelectric elements is used for lateral motion control and the bimorph actuation of piezoelectric elements is used for transversal motion control. Since the actuator has simple structure, it has good productivity and can be used with existing conventional assembly. Two piezoelectric layers are used for the microactuator. The use of two layers not only increases stiffness and generates large forces but also reduces driving voltage. Dynamic properties of the system are related to system parameters such as the natural frequency, the mass moment of inertia, and the damping ratio of the system. The frequency response analysis shows that the higher natural frequency, lower damping ratio and lower mass moment of inertia are required to achieve better performance of the actuator system. Those system parameters are related to the shape, size and material properties of the actuator and the slider. By modifying the shape of the actuator and choosing proper materials, we can achieve better performance of the system. To increase the natural frequency of the lateral actuator, increasing the cross section area of the lateral actuator or reducing the length of the lateral actuator is required. To reduce the mass moment of inertia of the positioning system, reducing the mass and the size of the slider is required. Since a conventional Pico size slider is used in this study, the value of the mass moment of inertia of the positioning system does not change. However, with this knowledge, using smaller and lighter sliders, or using head driven actuator designs can be considered. To increase the natural frequency of the transverse actuator, increasing the thickness of the actuator or reducing the length or density of the transverse actuator is required. Feedback control is used for precise control. Since the proposed actuator has good rise time and settling time but relatively high overshoots, the compensator is designed to limit overshoot to no more than 5 % . The proposed controllers in the closed-loop system compensate for disturbances. The microactuator improved performance of

high density hard disk drives by increasing servo bandwidth and decreasing flying height.

It should be noted that the piezoelectric actuator needs high voltage input to generate the required displacement. Modifying the structure of the piezoelectric microactuator, which needs less voltage input, is needed. A stack design can be used to reduce the driving voltage. However, increasing adhesive layers can affect the dynamics of the actuator system and the total actuator thickness is limited by the structure of the existing assembly. Further study of the effect of an adhesive layer and the total actuator thickness to the dynamics of the positioning system for hard disk drives is desirable. Experimental work for evaluating the damping of the actuator system is also needed including work related to the material science of piezoelectric materials in order to evaluate the damping effect caused by the heat generation of the piezoelectric materials. There is another problem associated with the controller design for the actuator system. In the controller design for the lateral control, the track seeking controller is used at low frequency part and the track following controller is used at high frequency part. However, the switching of the control mode is not considered in this study. More work could be done in the future for control system improvement.

APPENDIX A: NOMENCLATURE

Characters

A	coefficient of mode shape function
A_c	cross section area of the actuator
A	state space model system matrix
B	state space model system matrix
b	width of the actuator
C(s)	transfer function of a controller
c	damping constant of the lateral actuator
c_m	modal damping of the transverse actuator
D(s)	transfer function of the compensator
D	electric displacement vector
D	bending stiffness
d	piezoelectric strain constant matrix
d_{31}	piezoelectric strain constant
d_s	distance between the center of mass of the slider and the center of rotation in the lateral direction
E	electric field vector
e_{31}	piezoelectric stress coefficient
F	$n \times n$ state space model system matrix
F_m	modal force of the transverse actuator
F_1	modal force of the transverse actuator in the first mode
G	$n \times 1$ state space model input matrix
G	transfer function of a system
G_P	transfer function of the controller and piezoelectric actuator
G_V	transfer function of the controller and voice coil motor
H	$1 \times n$ state space model output matrix
h	thickness of the actuator

I	area moment of inertia
J	direct transmission term in state space model system
J	mass moment of inertia of the slider about the center of rotation
J_c	mass moment of inertia of the slider about the center of mass
J_a	mass moment of inertia of voice coil actuator
K	control law
K_t	torque constant for voice coil motor
k	equivalent spring constant of the lateral actuator
k_p	equivalent spring constant of the single piezoelectric layer of the lateral actuator
L	length of the transverse actuator
L_1	length of the lateral actuator
L_2	length between the center of lateral rotation and the head
M	bending moment of the bimorph actuator
M_p	overshoot of the system
m_s	mass of slider
P	force generated by the lateral actuator
P_p	force generated by the a single piezoelectric layer in the lateral direction
P_c	center of lateral rotation
p_3	equivalent input distributed loading
q_3	control force induced by external applied voltages
r	moment arm in the lateral direction
$\mathbf{S}$	strain tensor
$\mathbf{s}^E$	compliance matrix evaluated at a constant electric field.
$\mathbf{T}$	stress tensor
t	time
t_r	rise time of the system

U_{3m}	mode shape function
u_3	displacement
u	control input in the state space model system
u_V	control input to the controller for the voice coil motor
u_P	control input to the controller for the piezoelectric actuator
V	voltage
Y	Young's modulus
Y_p	Young's modulus of piezoelectric materials
Y	displacement output
z	a moment arm in transverse direction

Greek

$\boldsymbol{\varepsilon}^T$	dielectric tensor measured at constant stress T
η_m	modal participation factor
λ_m	eigenvalue of characteristic equation
μ	Poisson's ratio
ρ	mass density
ρ_p	mass density of piezoelectric materials
θ	rotational angle
ω	input frequency
ω_n	natural frequency
ω_m	modal natural frequency
ω_1	natural frequency in the first mode
ζ	damping ratio
ζ_m	modal damping ratio
ζ_1	damping ratio in the first mode

APPENDIX B: MATERIAL PROPERTIES OF PZT5

Property	Symbol	Unit	PZT501	PZT502	PZT503	PZT504	PZT505	PZT506	PZT507	PZT508
No of days after poling			**1**	**1**	**1**	**1**	**1**	**1**	**1**	**1**
Electrical - Low Field										
Relative Permittivity	$\varepsilon_r^T{}_{33}$		2000	1950	2100	2000	2600	2250	3900	3900
Relative Permittivity	$\varepsilon_r^T{}_{11}$				1800				3300	
Dielectric Loss	Tan δ		0.02	0.02	0.02	0.015	0.019	0.02	0.016	0.02
Resistivity (at approx 25°)	ρ el	Ωm	$>10^{11}$		50^{10}	50^{10}	50^{10}		10^{10}	
Resistivity (at 100°)	ρ el	Ωm	10^{11}							
Resistivity (at 200°)	ρ el	Ωm	10^{10}							
Electrical - High Field										
Increase in $\varepsilon^T{}_{33}$ @ 2KV/cm		%								
Dielectric Loss @ 2KV/cm	Tan δ									
Increase in $\varepsilon^T{}_{33}$ @ 4KV/cm		%								
Dielectric Loss @ 4KV/cm	Tan δ									
Electro-Mechanical										
Coupling Factors	k_p		0.600	0.645	0.680	0.640	0.720	0.700	0.700	0.710
	k_{15}		0.63	n/a	0.66					0.72
	k_{31}		0.34	0.35	0.38	0.37			0.39	0.41
	k_{33}		0.66	n/a	0.75	0.74			0.80	0.75
	k_t									
Charge Constants	d_{33}	$\times 10^{-12}$ C/N	405	450	500	450	610	545	700	720
or Strain Constants	d_{31}	$\times 10^{-12}$ C/N or m/V	-185	-195	-215	-200	-270	-225	-280	-315
	d_h	$\times 10^{-12}$ C/N	95	60						90
	d_{15}	$\times 10^{-12}$ C/N or m/V	564	n/a	515					750
Voltage Constants	g_{33}	$\times 10^{-3}$ Vm/N	22.9	25	24	25			20	18.5
or Stress Constants	g_{31}	$\times 10^{-3}$ Vm/N	-10.5	-11.5	-10	-12			-10	-9
	g_h	$\times 10^{-3}$ Vm/N	1.9	2						0.5
	g_{15}	$\times 10^{-3}$ Vm/N	36.4	n/a	33					
	$d_h g_h$	$\times 10^{-15}$	181	120						45
Frequency Constants	N_p	Hz.m	1950	1930	1975	2000	1900	1940	1925	1950
	N_1	Hz.m	1420	1400	1450				1400	1420
	N_3	Hz.m			1850	1900			1800	1880
	N_5	Hz.m			930					
	N_4	Hz.m	n/a	n/a						
	N_{31} or N_{33}	Hz.m	n/a	n/a						
	N_t	Hz.m								
	Hoop or N_t	Hz.m	890	78						
	N_t	Hz.m								
Compressive Strength		10^8 Pa			>600	>600			>600	
Tensile Strength		10^8 Pa			80	80			80	
Quality Factor	Q_m		75	80	75	75	60	65	65	55
Mechanical										
Compliances	$S^E{}_{33}$	$\times 10^{-12}$ m²/N	n/a	n/a	18	19			20	22
	$S^E{}_{11}$	$\times 10^{-12}$ m²/N	16.4	16.1	15	15	16.5	15.5	16	16.4
	$S^E{}_{12}$	$\times 10^{-12}$ m²/N								
	$S^E{}_{13}$	$\times 10^{-12}$ m²/N								
	$S^E{}_{55}$	$\times 10^{-12}$ m²/N			39					
	$S^E{}_{66}$	$\times 10^{-12}$ m²/N								
	$S^D{}_{33}$	$\times 10^{-12}$ m²/N	n/a	n/a						8.8
	$S^D{}_{11}$	$\times 10^{-12}$ m²/N	14.4	14.1						13.9
	$S^D{}_{12}$	$\times 10^{-12}$ m²/N								
	S_{66}	$\times 10^{-12}$ m²/N								
	$Y^E{}_{33}$	$\times 10^{10}$ N/m²	n/a	n/a						4.9
	$Y^E{}_{11}$	$\times 10^{10}$ N/m²	6.1	6.2						6.1
	$Y^D{}_{33}$	$\times 10^{10}$ N/m²	n/a	n/a						11
	$Y^D{}_{11}$	$\times 10^{10}$ N/m²	6.9	7.1						7
Poisson's Ratio σ			0.31	0.31	0.3	0.3			0.3	
Density	ρ	kg/m³	7600	7800	7800	7800	7830	8000	7800	7900
Thermal Data										
Curie Temperature	T_c	°C	330	350	285	270	285	300	165	220
Approx. Operating Temp.		°C								
Specific Heat		J/kg K			420	420			420	
Thermal Conductivity		W/m K			1.2	1.2			1.2	
Young's Modulus	E	Gpa								
Internal Friction	Q^{-1}	$\times 10^{-4}$								
Time Stability										
Coupling Factor	k_p	Relative change per time decade %	0.00	0.00	-0.50	-1.50			-0.60	
Permittivity	$\varepsilon^T{}_{33}$		-0.90	-3.60	-1.00	-2.00			-1.00	
Frequency	f		+0.1	+0.2	0.5	0.50			0.30	
	d_{33}		-2.90	-3.10						
Time Constant	ρεT/33 (25°C)	minute			>300	>25			>500	

References

[1] R.B. Evans, J.S. Griesbach 1999 “Piezoelectric microactuator for dual stage control” *IEEE Trans. Magn.* Vol. 35, No. 2, pp. 977-982.

[2] Y. Niu, W. Guo, G. Guo, E. Ong, K. Sivadasan, and T. Huang 2000 “A PZT micro-actuated suspension for high TPI hard disk servo systems*” IEEE Trans. Magn.* Vol. 36, No. 5, pp. 2241-2243.

[3] M. Kobayashi and R. Horowitz 2001 “Track seek control for hard disk dual-stage servo systems” *IEEE Trans. Magn.* Vol. 37, No. 2, pp. 949-954.

[4] S. Koganezawa and T. Hara 2001 “Development of shear-mode piezoelectric microactuator for precise head positioning” *FUJITSU Sci. Tech. J.,* Vol. 37, No. 2, pp. 212-219.

[5] Y. Soeno, S. Ichikawa, T. Tsuna, Y. Sato and I. Sato 1999 “Piezoelectric piggy-back microactuator for hard disk drive” *IEEE Trans. Magn.* Vol. 35, No. 2, pp. 983-987.

[6] H. Kuwajima and K. Matsuoka 2001 “Thin-film piezoelectric DSA for HDD” *IEEE Trans. Magn.* Vol. 38, No. 5, pp. 2186-2188.

[7] L.S. Fan, T. Hirano, J. Hong, P.R. Webb, W.H. Juan, W.Y. Lee, S. Chan, T. Semba, W. Imaino, T.S. Pan, S. Pattanaik, F.C. Lee, I. Mcfadyen, S. Arya, R. Wood. 1999 “Electrostatic microactuator and design considerations for HDD applications” *IEEE Trans. Magn.* Vol.35, No. 2, pp. 1000-1005.

[8] M. A. Jabbar, W.i Jia, and J.Yang 2004 “Simulation and optimization of an electrostatic microactuator for HDD head positioning” *IEEE Trans. Magn.* vol. 40, No. 4, pp. 3174-3176.

[9] B. Kim and K. Chun 2001 “Fabrication of an electrostatic track-following micro actuator for hard disk drives using SOI wafer”. *J. Micromech. Microeng.* Vol. 11, pp.1–6.

[10] H. Toshiyoshi, M. Mita, and H. Fujita 2002 “A MEMS piggyback actuator for hard-disk drives” *J. Microelectromechanical systems,* Vol. 11, No. 6, pp. 648-654.

[11] S.l Lim, J. Park, S.k Choi, and Y. Park 2001 “Non-contact start/stop motion control of HDD suspension using shape memory alloy actuators” *Smart Mater. Struct.* Vol. 10, pp.

1069–1077.
[12] N. Tagawa, K. Kitamura, and A. Mori 2002 “Development of novel PZT thin films for active sliders based load/unload on head demand systems” *Microsystem Technologies* Vol. 8, pp. 133-138.
[13] M. Kurita and K. Suzuki 2004 “Flying-height adjustment technologies of magnetic head sliders” *IEEE Trans. Magn.* Vol. 40, No. 1, pp. 332-336.
[14] N. Tagawa, K.I. Kitamura, and A. Mori 2003 “Design and fabrication of MEMS-based active slider using double-layered composite PZT thin film in hard disk drives” *IEEE Trans. Magn.* Vol. 39, No. 2, pp. 926-931.
[15] B. Liu, Y. L. Zhu, Y.H. Li, W. H, Q.F. Leng and G. Sheng 1999 “An experimental study of slider vibration in nanometer spaced head-disk interface” *IEEE Trans. Magn*. vol. 35, No. 5, pp. 2463-2465.
[16] V. Venkataramanan, B.M. Chen, T.H. Lee, G. Guo 2002 “A new approach to the design of mode switching control in hard disk drive servo systems” *Control Engineering Practice* Vol. 10, pp. 925–939.
[17] X. Liu, A. Li, W. Clegg, F. L. Jenkins, and P. Davey 2002 ”Head-disk spacing variation suppression via active flying height control” *IEEE Trans. Instrumentation and measurement,* Vol. 51, No. 5, pp. 897-901.
[18] H. S. Tzou 1989 “Development of a light-weight robot end-effector using polymeric piezoelectric bimorph” *IEEE international conference on robotics and automation*, pp. 1704-1709.
[19] G. F. Feanklin, J. D. Powell 1995, A. Emami-Naeini, “Feedback control of dynamic systems”, Addison Wesley, Reading, Mass.
[20] Albert P. Pisano 2005 “MEMS Solutions for Data Storage”, Berkeley Sensor & Actuator Center, Berkeley, California.
[21] H. S. Tzou 1993 “Piezoelectric Shells: Distributed Sensing and Control of Continua” Kluwer Academic Publishers Dordrecht, The Netherlands.

VITA

The author was born in Seoul, South Korea, on February 26, 1976. She entered the Ajou University in the Spring of 1996 and received her Bachelor of Science in Mechanical Engineering in the Fall of 2000. Since the Fall of 2003 she has been working toward her Master of Science in Mechanical Engineering.

Publications:

W.K. Chai, Y. Han, K. Higuchi, H.S. Tzou, 2005, "Micro-actuation characteristic of rocket conical shell sections," *Journal of Sound and Vibration*. (to appear)

J.G. DeHaven, Y. Han, H.S. Tzou, 2005, "Transition of Neural Signal on Cylindrical Shells with Various Curvatures," *ASME 2005 International Design Engineering Technical Conferences & Computers and Information in Engineering Conference,* Long Beach, California, USA, September 23-28, 2005. (Paper No. DETC2005-85153)

Younghee Han

December 15, 2005